

SIMULATION OF THE START UP PHASE OF METAL
HALIDE LAMPS

BY

ANANTH NUGGEHALLI BHOJ

B.Tech, Indian Institute of Technology, Madras, 2001

THESIS

Submitted in partial fulfillment of the requirements
for the degree of Master of Science in Chemical Engineering
in the Graduate College of the
University of Illinois at Urbana-Champaign, 2004

Urbana, Illinois

ABSTRACT

Metal halide lamps are widely used for interior and exterior lighting due to their favorable color characteristics and high luminous efficiencies. This thesis reports on a computational investigation into the startup processes of metal halide lamps. Parametric studies were performed using zero-dimensional and two-dimensional models to determine the effect of varying pressure, composition, and applied voltage on electrical breakdown times in these lamps. Spatial dynamics of breakdown were visualized using the two-dimensional model. Lower pressures and higher voltages were found to reduce breakdown times by increasing available E/N . In Ar/Xe gas mixtures, breakdown occurs more rapidly than in either pure gas.

An ambipolar module for charged particle transport was developed for the two-dimensional model in order to continue calculations deep into the glow phase. Energy deposition in the gas is low during breakdown. After the breakdown event, the plasma density and energy deposition increase. To capture the resulting hydrodynamic effects, the plasma dynamics code was interfaced to a modified fluid dynamics code with which Navier-Stokes' equations are solved. In the glow phase, the rise in gas temperature leads to initiation of transient convective fields. Small changes in E/N resulting from convection have rapid and significant effect on plasma properties.

ACKNOWLEDGEMENTS

I would like to express my gratitude to my adviser, Prof. Mark J. Kushner for his constant support and guidance during the course of this project.

I am also thankful to the past and present members of the group – Rajesh Dorai, Alex Vasenkov, Richard Moss, Pramod Subramonium, Arvind Sankaran, Kapil Rajaraman, Vivek Vyas, Shane Stafford, Ramesh Arakoni, Ankur Agarwal and Kelly Collier.

I am deeply grateful to my parents and my brother and relatives for their love and encouragement.

TABLE OF CONTENTS

1. INTRODUCTION	1
1.1 Metal Halide Lamps.....	1
1.2 Specifications and Applications.....	2
1.3 The Startup Process.....	3
1.4 Experimental and Modeling Studies.....	5
1.5 Overview.....	8
1.6 Figures.....	9
1.7 References.....	11
2. DESCRIPTION OF THE BREAKDOWN MODELS	13
2.1 Introduction.....	13
2.2 The Zero-Dimensional Model.....	13
2.3 The Two-Dimensional Model – LAMPSIM.....	15
2.3.1 Charged species and neutral transport	15
2.3.2 Electron energy transport.....	17
2.3.3 Gas and surface chemistry	18
2.4 Limitations	20
2.5 Figures.....	21
2.6 References.....	22
3. INVESTIGATION OF BREAKDOWN IN Ar/Xe MIXTURES.....	24
3.1 Introduction.....	24
3.2 Lamp Geometry and Reaction Chemistry.....	24
3.3 Breakdown Trends using the Zero-Dimensional Model.....	25
3.4 Results from the Two-Dimensional Model.....	28
3.4.1 Spatial breakdown dynamics	29
3.4.2 Effect of varying composition	33
3.4.3 Effect of varying pressure.....	35
3.4.4 Effect of varying applied bias	36
3.5 Concluding Remarks.....	37
3.6 Figures.....	39
3.7 References.....	68
4. HYDRODYNAMIC EFFECTS DURING STARTUP PHASE	69
4.1 Introduction.....	69
4.2 The Ambipolar Module.....	70
4.3 The Fluid Dynamics Module	72
4.4 Interfacing the Fluid Module and LAMPSIM	74
4.4.1 Automated fluid mesh generation.....	74
4.4.2 Interpolation setup	75
4.5 Interaction of Plasma Dynamics and Hydrodynamics.....	77
4.5.1 Dynamics of gas temperature.....	77
4.5.2 Effect on plasma properties	79

4.6 Conclusions.....	80
4.7 Figures.....	81
4.8 References.....	91
5. CONCLUSIONS.....	92
APPENDIX A: KINETICS OF Ar/Xe MIXTURES.....	94
A.1 List of Species.....	94
A.2 Ar/Xe Reaction Mechanism.....	94
A.3 References.....	99

1. INTRODUCTION

1.1 Metal Halide Lamps

Metal halide lamps are part of the family of high intensity discharge (HID) lighting sources that includes high-pressure mercury lamps and sodium vapor lamps.¹ These lighting sources operate on the principle of electron impact ionization of the enclosed gas to produce radiation, different from incandescent technology that utilizes resistively heated elements to emit light in the visible spectrum. The advantages of high efficiency and favorable color characteristics have contributed to expanding the market for HID lamps.

A typical metal halide lamp is shown in Figure 1.1.² The outer jacket encloses an inner lamp envelope or arc tube. The lamp envelope is typically made of quartz, ceramic, or polycrystalline alumina. There are two pinch-sealed electrodes, usually made of low work function, high-temperature resistant material such as tungsten, and the inter-electrode distance ranges from 1 to 5 cm depending on the wattage and application.

Gas-fills usually consist of a rare gas like Argon at a few tens to a hundred Torr and a small dose of metal halides and/or mercury at a few mTorr vapor pressure when the lamp is cold. Metal halide salts are usually added in order to improve color rendering and color temperature. The arc tube may be surrounded by a shroud to provide protection in the event of an explosion and also helps redistribute heat. The outer jacket provides mechanical means for mounting electrical inlets and the socket. The space in between the arc tube and the outer jacket may either be vacuum or filled by low-pressure nitrogen to facilitate cooling mechanisms that influence the arc tube wall temperature.

Usually, electrical ballasts are required to start the lamp and regulate its operation. Ballasts are specifically designed for each type of lamp, depending on the lamp geometry and gas-fill. At steady state operating conditions, the lamp would be a multiatmosphere thermal arc close to local thermal equilibrium.

1.2 Specifications and Applications

Lamps are compared and rated on the basis of their color rendering indices, efficiencies, and lifetimes.³ Color rendering is measured in terms of the Correlated Color Temperature (CCT) and the Color Rendering Index (CRI), a rating system recognized by the Illuminating Engineering Society. CRI is rated on a scale from 1 to 100, 100 being associated with natural daylight. Color rendering describes how the light source illuminates objects as compared to natural daylight. Metal halide lamps usually emit color very close to white light while that from sodium lamps is usually yellowish. Thus, the CRI of metal halide lamps is around 91 while a mercury vapor lamp has a CRI of around 55. Higher color temperatures describe a visually cooler and bluer light source. Typical color temperatures are 3000 K for an incandescent source, around 4500 K for a metal halide lamp, and about 5100 K for natural daylight.

The efficiency of a lamp is a measure of the light emitted by a lamp to the electrical power consumed. Metal halide lamps have a much higher efficiency of about 115 lumens/watt (lm/W) compared to about 60 lm/W for mercury vapor lamps. Though sodium vapor lamps have a comparatively higher efficiency up to 140 lm/W, they are not often favored because of their poor color rendering characteristics.

The definition of average lifetime varies across different types of lamps. The most common test for HID lamps is to burn the lamps on a cycle of 10 h on and 2 h off, and measure the time at which 50% of the lamps have failed. Metal halide lamps usually have a rated life of 10 000 - 15 000 h. Conventional incandescent lamps and compact fluorescent lamps are generally rated for a life of 2 000 h and 10 000 h respectively.

Metal halide lamps are becoming common sources of outdoor, sports, and commercial interior lighting. Wherever lighting of large areas is required and long hours of operation are required, metal halide lamps are a good option to consider. Color temperature characteristics of metal halide lamps being similar to daylight enable colors to be reliably reproduced. The development of low wattage lamps has led to newer applications in office, retail, and residential environment lighting. Metal halide lamps have been developed for use as automotive headlamps as well.

1.3 The Startup Process

The startup process of a lamp is typically categorized into different phases that have unique characteristics: breakdown of the gas, cold cathode/glow phase, glow-to-arc transition, and the thermionic arc phase.⁴ During the early startup phase, the conditions in the lamp are similar to the development of a moderate pressure glow discharge.

The breakdown phase is characterized by a time lag between the application of voltage to the lamp and the time by which it becomes conductive. There are two components to the breakdown time lag. The formative time lag is the time required to avalanche the gas to a conductive phase and is a function of the lamp geometry and E/N (electric field/gas number density). This is usually smaller than the statistical time lag,

which is the average time to seed the gas-fill with electrons to initiate the discharge. The breakdown process itself is thought to occur by a cumulative ionization process, which depends on availability of free electrons to start with. The statistical time lag can have a wide distribution in the absence of starting aids.

After breakdown, the lamp enters a cold cathode phase if condensed mercury/metal halide salts are present. In a cold cathode phase the mercury and metal halide salts condensed on the electrode are vaporized and then ionized. This results in decreased impedance, which is temporary as the source of mercury is soon depleted. The lamp then enters a glow discharge phase. During the glow discharge phase, the main source of secondary electrons is ion bombardment, which sputters the cathode and eventually heats it. A cold cathode glow discharge in low-wattage metal halide lamps has an abnormal glow property, wherein the voltage across the discharge increases as the current increases. High-wattage lamps exhibit normal glow behavior wherein the voltage across the lamp remains constant with varying current.

Beginning in the glow phase, the power deposition is sufficient to start heating the gas. When ion bombardment heats the cathode to a sufficiently high temperature, thermionic emission of electrons from the cathode becomes significant and marks the glow-to-arc transition. Thermionic emission soon dominates over other secondary source terms and a thermal arc develops. Steady state operation is reached over a few minutes and pressure in the arc tube can be several atmospheres. Figure 1.2 illustrates the variation of impedance at different stages during startup.

1.4 Experimental and Modeling Studies

The expanding market for HID lamps has motivated research into improving the reliability of operation and lifetime of these lamps. Experimental and modeling studies undertaken by several investigators have focused on higher lamp efficiency, lumen maintenance, enhanced optical properties, and shorter breakdown times for cold and warm starting. These studies have added to our understanding of the complex physics and chemistry that characterizes the different stages of startup in these lamps.

Felsenthal and Proud measured breakdown time lags in different gases and developed a theory for the formative time lag.⁵ Strategies have been developed for reducing statistical lag times by seeding the discharge such as the use of auxiliary electrodes, addition of radioactive Kr⁸⁵, and external ultraviolet (UV) sources. While one of the objectives is to reduce breakdown time, another is to keep the breakdown voltage low. High starting voltages reduce lamp life by sputtering electrode material leading to permanent wall tube darkening.⁴ Seeding of the discharge reduces the excess voltage necessary to breakdown the gas. Researchers have studied the use of ultraviolet light (UV) in reducing the breakdown time lag to decrease the overall ignition time.¹ Byszewski and Budinger studied the statistical variation of breakdown time with and without a UV enhancer.⁶ The presence of an external UV source led to a decrease in the breakdown time by providing a means of generating seed electrons. The use of starter electrodes used in earlier versions of high wattage metal halide lamps as a means of seeding electrons has been replaced by the use of pulse-start technology that was common in low wattage lamps.

Lumen loss resulting from wall blackening due to the deposition of sputtered electrode material during startup could be as high as 50% at the end of the lamp life.⁷ The transparency of the arc tube and the consequences of cyclic operation have been studied. Cyclic operation results in significantly higher lumen loss compared to continuous operation. Gregor et al., studied the causes of arc tube darkening and reported sputtering processes at the electrode during startup to be a primary cause of wall blackening.⁴ The composition and pressure of the gas fill affects breakdown voltage. Bergmann⁸ reported on the influence of impurities on pre-breakdown phenomena in the gas phase of discharge lamps containing mercury. The design of formed arc tubes enable higher fill pressures and uniformity over the older pinched arc sealed tubes. Improved temperature control has translated into better color properties.

Pitchford et al.⁹, developed a one-dimensional model to investigate the breakdown and glow phases during startup. Conditions needed to sustain the cold cathode discharge after the breakdown event has occurred have been modeled. It was found that the voltage necessary to sustain a glow discharge is dependent on the source impedance, the gas composition and the plasma density created by the breakdown event. Lay et al.¹⁰, using a two-dimensional model found that the capacitance had a significant effect on breakdown dynamics.

Restarting of warm lamps usually requires a much larger voltage as the pressure in the lamp is still high. High voltages pose risks of external arcing. Novel methods have been developed in order to circumvent the need for very large starting voltages. The use of controlled dimming is one technique.^{11, 12} When the switch is turned off, the voltage applied to the gas fill is decreased while still maintaining a conductive path between the

electrodes. It might take several minutes for the pressure in the lamp to reduce as the metal vapors condense and the lamp cools down. If the lamp switch is turned on again within this interval, raising the ballast to full power enables a much faster restart time for the warm lamp due to the presence of the low-level discharge. The design of electronic ballasts is another major area of research.¹³ Optimized breakdown voltage waveforms reduce electrode sputtering. Lower starting voltages lead to simpler ballast designs.

Several investigators have studied the glow-to-arc transition.^{14, 15} Luijks and van Vilet¹⁵ determined design rules to optimize glow-to-arc transitions for metal halide lamps. They found that maximizing the glow current, gas-fill pressure, and glow surface area of the electrode and minimizing the glow voltage, electrode heat capacity, and electrode work function optimizes glow-to-arc transition.

Metal halide lamps usually have additives in the form of small doses of metal halide or lanthanide halide salts.³ The role of these additives is primarily to impart the desired color characteristics in terms of CRI and CCT. Examples of these additives are NaI/DyI₃ or NaI/ScI₃ with a small dose of Hg. These additives could be present in the lamp in a condensed phase or in a gaseous phase. When the lamp is being operated, these additives undergo a variety of changes. The rise in wall temperature causes condensed species to vaporize. Power deposition in the plasma results in the dissociation of the metal halides and excitation of the free metal atoms. Recombination of the free metal atoms with the halide species near the walls completes the cycle. The halide species could also combine with sputtered tungsten on the wall in what is referred to as wall cleaning.¹⁶ Gaseous homogeneous and heterogeneous complexes of these metal halides may also form. Thermochemical modeling to support development of metal halide lamps

found enhanced chemical vapor transport of metal species and an increased metal concentration that could be utilized to modify color rendering properties and the efficiency of light generation.¹⁷ Ceramic metal halide lamps reduce sodium loss limiting color shift.

More recently, modeling studies have been undertaken in the context of mercury vapor lamps. Bashlov et al.¹⁸, used a steady state collisional-radiative model describing the middle phase of startup. Stambouli et al.¹⁹, studied the lamp-network interaction during the warm up phase of a high-pressure mercury discharge lamp that was described by a local thermodynamic equilibrium concept. Tougher environmental legislations have ensured initiatives in the lighting industry to reduce and eventually eliminate the use of toxic materials such as mercury and radioactive additives such as Kr⁸⁵.²⁰ Recent studies have focused on zinc as a suitable candidate for replacing mercury in metal halide lamps.^{21, 22}

1.5 Overview

This work describes a computational investigation into the breakdown and early glow phase during the startup process of HID lamps. The models used in this study are described in Chapter 2. Breakdown times are computed using these models for starting in Ar/Xe mixtures to facilitate comparison to experiments and are described in Chapter 3. Hydrodynamic effects resulting from gas heating in the early post-breakdown phase affect the plasma dynamics. A fluid model is interfaced to the plasma dynamics model to describe hydrodynamic effects and is presented in Chapter 4. A brief conclusion is provided in Chapter 5.

1.6 Figures

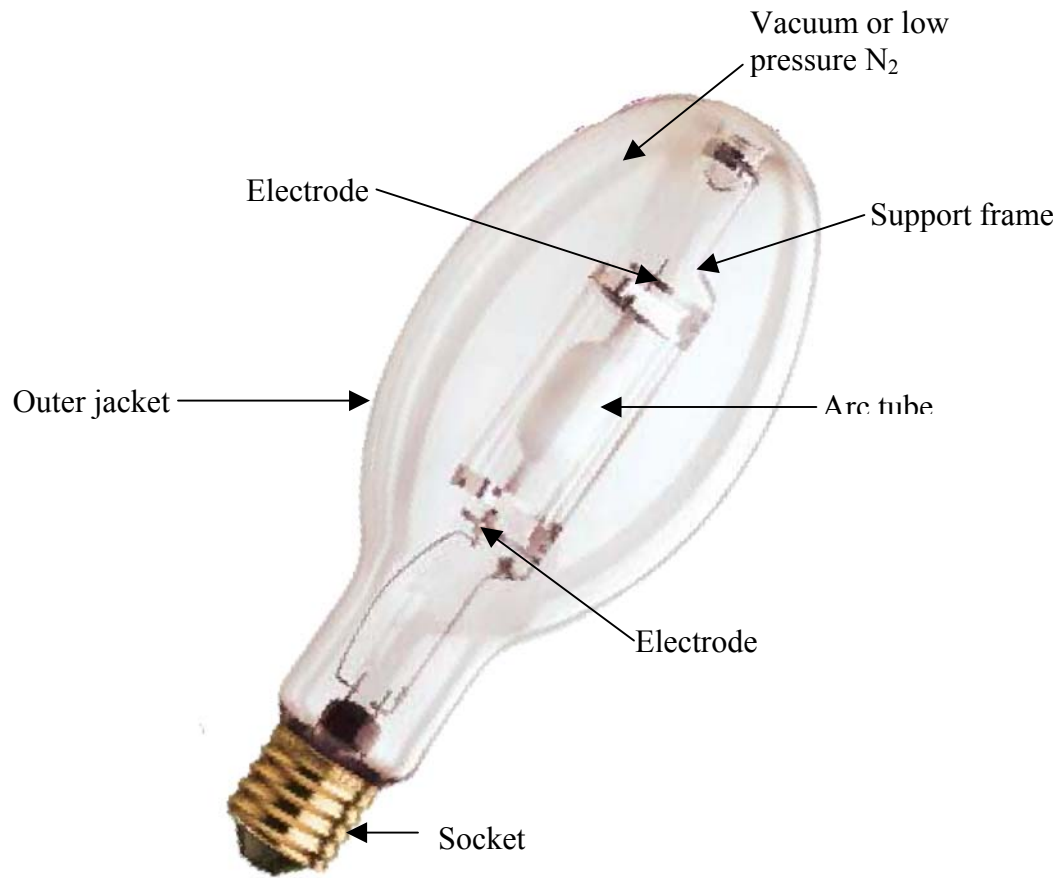


Figure 1.1 Construction of a metal halide lamp.²

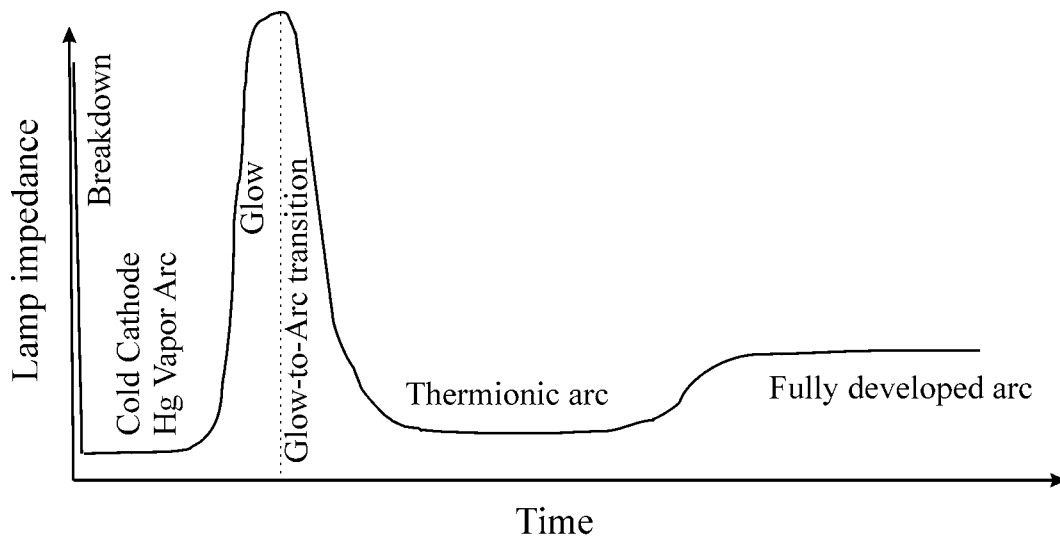


Figure 1.2 HID lamp impedance at different stages during startup.⁴

1.7 References

- 1 J. F. Waymouth, *Electric Discharge Lamps* (MIT Press, Cambridge MA, 1971).
- 2 GE metal halide lamps product brochure 20654 (2003).
- 3 *Lamps and Lighting* Edited by S. T. Henderson, and A. M. Marsden (Crane, Russack and Company, Inc., New York, 1972).
- 4 P. D. Gregor, Y. M. Li, A. B. Budinger, and W. W. Byszewski, *Journal of the Illuminating Engineering Society* **25**, 150 (1996).
- 5 P. Felsenthal and J. M. Proud, *Phys. Rev.* **139**, A1796-A1804 (1965).
- 6 W. W. Byszewski and A. B. Budinger, *Journal of the Illuminating Engineering Society*, 70 (Summer 1990).
- 7 W. W. Byszewski, Y. M. Li, A. B. Budinger, and P. D. Gregor, *Plasma Sources Sci. Technol.* **5**, 720 (1996).
- 8 G. Bergmann, *Lighting Res. Technol.* **10**, 33 (1978).
- 9 L. C. Pitchford, I. Peres, K. B. Liland, J. P. Boeuf, and H. Gielen, *J. Appl. Phys.* **82**, 112 (1997).
- 10 B. M. Lay, R. S. Moss, S. Rauf, and M. J. Kushner, *Plasma Sources Sci. Technol.* **12**, 8 (2003).
- 11 D. Smith and H. Zhu, *Journal of the Illuminating Engineering Society* **22**, 27 (1993).
- 12 R. G. Gibson, *J. Illum. Eng. Soc.* **23**, 19 (1994).
- 13 N. Fukumori, H. Nishimura, K. Uchihashi, and M. Fukuhara, *Journal of the Illuminating Engineering Society* **24**, 41 (1995).
- 14 J. F. Waymouth, *Journal of the Illuminating Engineering Society* **17**, 166 (1987).

- 15 G. M. J. F. Luijks and J. A. J. M. van Vliet, *Lighting Res. Technol.* **20**, 87 (1988).
- 16 R. J. Campbell, *High Temperature Science* **1**, 303 (1969).
- 17 K. Hilpert and U. Niemann, *Thermochimica Acta* **299**, 49 (1997).
- 18 N. Bashlov, G. Zissis, K. Charrada, M. Stambouli, V. Milenin, and N. Timofeev,
J. Phys. D: Appl. Phys. **27**, 494 (1994).
- 19 M. Stambouli, K. Charrada, C. Costache, and J.-J. Damelin-court, *IEEE*
Transactions on Plasma Science **27**, 646 (1999).
- 20 OSRAM Sylvania "The Use of Mercury in Efficient Electric Lamps - An Update"
<http://www.sylvania.com/press/03132001.html> (2001).
- 21 M. Born, *J. Phys. D: Appl. Phys.* **34**, 909 (2001).
- 22 M. Born, *Plasma Sources Science and Technology* **11**, 55 (2002).

2. DESCRIPTION OF THE BREAKDOWN MODELS

2.1 Introduction

In this chapter, modeling capabilities developed to address the breakdown phase of startup are described. Zero-dimensional and two-dimensional models are used to analyze the breakdown process. The zero-dimensional model is presented in Section 2.2. The two-dimensional model captures the spatial dynamics leading to breakdown. An overview of the two-dimensional model is presented in Section 2.3.

2.2 The Zero-Dimensional Model

A plasma chemistry simulator GLOBAL_KIN¹ was adapted to study the breakdown problem. The schematic representation of this model is shown in Figure 2.1. There are three main modules: a plasma chemistry module, a circuit module, and a Boltzmann equation module. Based on the reaction mechanism, the plasma chemistry module constructs differential equations for the evolution of species densities and electron temperature. The circuit module is used to simulate the input voltage waveform and provide the required E/N in the plasma. The source terms for gas phase reactions are obtained from species concentrations and reaction rate coefficients using

$$\frac{dn_i}{dt} = \sum_j \left\{ (a_{ij}^2 - a_{ij}^1) k_j \prod_1 n_1^{a_{ij}^1} \right\} \quad (2.1)$$

where a_{ij}^1 and a_{ij}^2 are left-hand side and right-hand side stoichiometric coefficients of species i in reaction j , n_i is the density of species i , and k_j is the rate constant of reaction j , which depends on gas temperature and is calculated using Arrhenius expressions for reactions involving only gas phase species. The rate constants for electron impact

reactions are obtained as a function of the electron temperature by solving the two-term spherical harmonic expansion for Boltzmann's equation for electron energy distribution (EEDs) and parameterizing over a range of E/N. The external circuit consists of a ballast resistor and a storage capacitor that is initially charged up to the applied voltage. Electron temperature is determined by energy gained from Joule heating and energy lost in elastic and inelastic collisions,

$$\frac{d}{dt} \left(\frac{3}{2} n_e k_B T_e \right) = \vec{j} \cdot \vec{E} - \sum_i \frac{3}{2} n_e v_{mi} \left(\frac{2m_e}{M_i} \right) k_B (T_e - T_i) - \sum_l n_e k_l N_l \Delta \varepsilon_l \quad (2.2)$$

where n_e is the electron density, T_e is the electron temperature, \vec{j} and \vec{E} are current density and electric field in the discharge, respectively. v_{mi} is the electron momentum transfer collision frequency with species i , m_e is the electron mass, M_i and T_i are the mass and temperature of species i . For the i^{th} electron impact process, k_i is the reaction rate coefficient, N_i is the density of the heavy species collision partner, and $\Delta \varepsilon_i$ is the change in electron energy.

The average gas temperature is obtained taking into account heating from elastic and inelastic collisions with electrons, enthalpy of heavy particle reactions and heat transfer to surfaces,

$$\frac{d}{dt} (N c_p T_g) = \sum_i \frac{3}{2} n_e v_{mi} \left(\frac{2m_e}{M_i} \right) k_B (T_e - T_i) + \sum_j n_e k_j N_j \Delta \varepsilon_j - \sum_j \Delta H_j R_j - h_{\text{eff}} \frac{T_g - T_w}{d_{\text{gap}}} \quad (2.3)$$

where N is the total gas density, c_p is the specific heat, ΔH_j and R_j are the change in enthalpy and rate of j^{th} reaction, h_{eff} is the effective heat transfer coefficient to discharge walls having temperature T_w , and d_{gap} is the inter-electrode separation.

This set of ordinary differential equations is then integrated in time using VODE, a stiff equation solver. The experimental voltage waveform can be fed as the input and breakdown time is signified when gap voltage drops by more than 5% of its maximum value.

2.3 The Two-Dimensional Model - LAMPSIM

In this section, the two-dimensional model, LAMPSIM, will be described. A schematic of this model is shown in Figure 2.2. While the detailed description of the algorithms used in the model are found elsewhere^{2, 3}, the principal features will be presented here. The commercial mesh generator, Skymesh2⁴, is used to create a 2-D representation of the lamp geometry and generate the unstructured mesh. The mesh is kept static through the entire simulation. The geometry module reads in the mesh and performs the geometry computations required in other modules.

2.3.1 Charged species and neutral transport

Variables describing the breakdown process include the electric potential, computed over the entire geometry, species densities and fluxes, and electron and gas temperatures computed only in the interior region of the quartz tube. Surface charge is computed only on dielectric materials. Fundamental equations solved are

$$-\nabla \cdot \epsilon \nabla \Phi = \sum_j n_j q_j + \rho_s \quad (2.4)$$

$$\frac{\partial N_i}{\partial t} = -\bar{\nabla} \cdot \bar{\phi}_i + S_i \quad (2.5)$$

$$\frac{\partial \rho_s}{\partial t} = \sum_i -\nabla \cdot (q_i \bar{\phi}_i (1 + \gamma_i)) - \nabla \cdot (\sigma (-\nabla \Phi)) \quad (2.6)$$

where $\varepsilon, \Phi, \rho, N, D, \mu, \phi, \gamma, \sigma, S$, and q refer to the permittivity, electric potential, charge density, species number density, diffusion coefficient, mobility, species flux, secondary emission coefficient, conductivity of solid materials, source terms, and elementary charge respectively. The subscript denotes the identity of the species. Poisson's equation (Equation 2.4) describing the electric potential, transport equations (Equation 2.5) describing conservation for the charged species, and surface charge balance (Equation 2.6), are solved as a simultaneous set of equations.

Fluxes for charged species are formulated using the Scharfetter-Gummel technique.⁵ In this method, the flux between mesh points i and $(i+1)$ separated by Δx is given by

$$\bar{\phi}_{i+1/2} = \alpha \bar{D} \left(\frac{n_{i+1} - n_i \exp(\alpha \Delta x)}{1 - \exp(\alpha \Delta x)} \right) \quad (2.7)$$

where α is given by

$$\alpha = \frac{\left(\frac{q}{|q|} \right) \bar{\mu} \left(\frac{\Phi_{i+1} - \Phi_i}{\Delta x} \right)}{\bar{D}} \quad (2.8)$$

and $\bar{\mu}$ and \bar{D} are the average mobility and diffusion coefficient in the interval.

The source function includes gain and loss terms due to gas phase and surface chemistry.

The solution technique for solving Equations (2.4)-(2.6) consists of discretizing the governing equations using finite volume techniques and employing an implicit Newton's method to integrate in time using a numerical package, *dslucs*, obtained from the SLAP Sparse Matrix Library.^{6,7}

Neutral transport is mainly diffusive (Equation 2.9) and each neutral species i is tracked. S_i denotes source terms from gas and surface chemistry.

$$\frac{dN_i}{dt} = -D_i \nabla N_i + S_i \quad (2.9)$$

Neutral densities are updated implicitly in a time splicing manner using successive over-relaxation techniques following update of charged species densities.

The circuit model provides the interface to the external circuit. Boundary conditions for potential are calculated using the applied bias to the metal surfaces. A ballast resistor is in series with the lamp. The breakdown criterion is the time at which gap voltage drops by 5% of its peak.

2.3.2 Electron energy transport

To obtain the electron temperature, the electron energy equation is solved for average electron energy ε ,

$$\frac{d}{dt}(n_e \varepsilon) = \vec{j} \cdot \vec{E} - n_e \sum_i N_i \kappa_i - \nabla \cdot \left(\frac{5}{2} \varepsilon \vec{\phi}_e - \lambda \nabla T_e \right) \quad (2.10)$$

$$\vec{j} = q \vec{\phi}_e$$

where T_e is the electron temperature defined as $(2\varepsilon/3)$, n_e is the electron density, k_i is the rate coefficient for power loss for collisions of electrons with species i having density N_i , λ is the thermal conductivity, and $\vec{\phi}_e$ is the electron flux. This equation is implicitly integrated in time using the successive over-relaxation technique. The electron energy transport coefficients and rate coefficients used above are obtained by solving Boltzmann's equation for the electron energy distribution using a two-term spherical harmonic expansion and parameterizing over a range of E/N. The table of transport coefficients as a function of ε is thus constructed and interpolated during the solution of the electron energy equation.

2.3.3 Gas and surface chemistry

Gas phase chemistry contributes to source terms in charged species and neutral transport equations. Source terms due to electron impact reactions and heavy particle collisions are included. Source terms are similar to Equation (2.1) but are computed at each node in the mesh depending on the local electron and gas temperatures. Rate coefficients for electron impact reactions are computed in the electron energy transport module and expressions for heavy particle reactions using gas temperatures are normally of the Arrhenius form.

Seeding of electrons far away from the avalanche is possible due to photons from excited species in the ionized regions. A radiation transport module calculates sources due to photoionization,

$$S_{k,j}(\vec{r}) = N_k(\vec{r}) \int N_j(\vec{r}') \sigma_{k,j} G_j(\vec{r}', \vec{r}) d^3\vec{r}'$$

$$G_j(\vec{r}', \vec{r}) = \frac{\exp(-|\vec{r}' - \vec{r}|/\lambda_j)}{4\pi|\vec{r}' - \vec{r}|^2} \quad (2.11)$$

where $S_{k,j}(\vec{r})$ is the photoionization source for species k at location \vec{r} due to photons emitted from species j at location \vec{r}' , N refers to species densities, $\sigma_{k,j}$ is the photoionization cross section for species k , and the Green function $G_j(\vec{r}', \vec{r})$ is used to account for view angles that might block radiation. For the Ar/Xe reaction mechanism in this study, resonant radiation from Ar(4s) was the photoionization source and a photoionization cross section of 100 \AA^2 was used for Xe.

The surface chemistry module uses a flux-in/flux-out boundary condition. Of the total species flux striking a surface, a fraction can be specified to disappear and produce another species. For instance, an excited species can be designated to disappear on

striking the surface and reappear as the ground state species by imparting its energy to the surface,

$$\phi_i = \phi_i^0(1 - \alpha_i) + \sum_k \phi_k^0 \beta_{k,i} \quad (2.12)$$

where ϕ_i^0 is the flux of species i into the surface, α_i is the fraction of that flux that disappears at the surface, and $\beta_{k,i}$ is the fraction that gets converted to species k that is returned from the surface. Another example would be secondary electron emission from surfaces due to ion bombardment. In this case, secondary emission coefficients for the respective ion species on the surface material are used to specify the fraction of species influx emitted as secondary electrons.

External sources such as UV flashlamps are used to generate seed electrons and reduce the statistical lag time component of breakdown times. An external UV module evaluates source terms due to energetic external UV photons. Source terms would comprise photoionization in the gas and photoemission from electrode surfaces. Photoemission from surfaces due to internal photons emitted by excited species in the discharge volume is also included.

Trajectories of secondary electrons emitted from the surfaces are followed with the Electron Monte Carlo Simulation (EMCS).⁸ The EMCS is performed on a separate submesh appropriately defined near the electron-emitting surface. Particles are released from electron emitting nodes on the submesh and their trajectories are computed using electric fields interpolated from the main mesh. Those electrons that have energy below a certain threshold are removed from the simulation. The results of the EMCS are electron impact source functions and sources of secondary electrons resulting from these beam electrons. EMCS is called at regular intervals and sources of electron impact and

secondary emission are held constant between calls. The source functions are obtained by computing EEDs of the beam electrons and their progeny in the EMCS, and convolving the EEDs with cross sections.

2.4 Limitations

Zero-dimensional models assume a uniform electric field in the discharge that is not expected to be accurate under all conditions. It is, however, a computationally simpler approach to obtain quick estimates of the breakdown time. The 2-D model captures the spatial dynamics of the breakdown process. In reality, the lamp structures have 3-D attributes that are only approximated in the 2-D representation of the geometry.

2.5 Figures

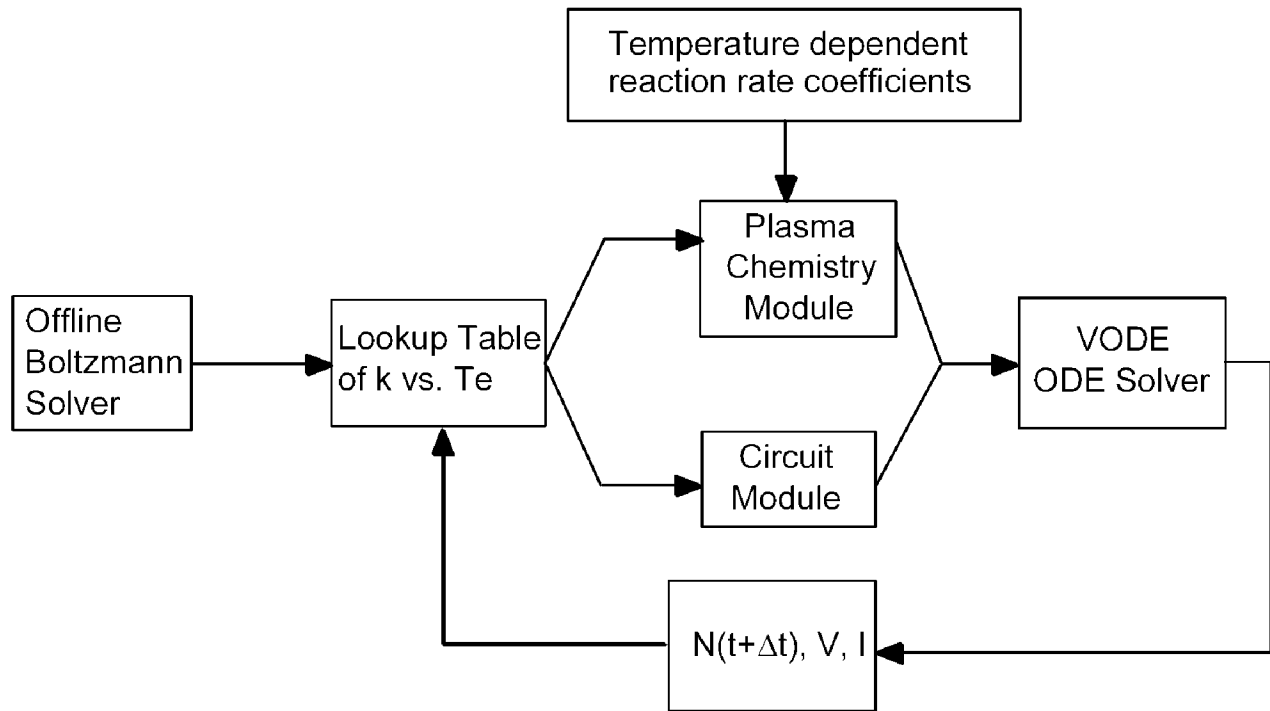


Figure 2.1 Block diagram of the zero-dimensional model.

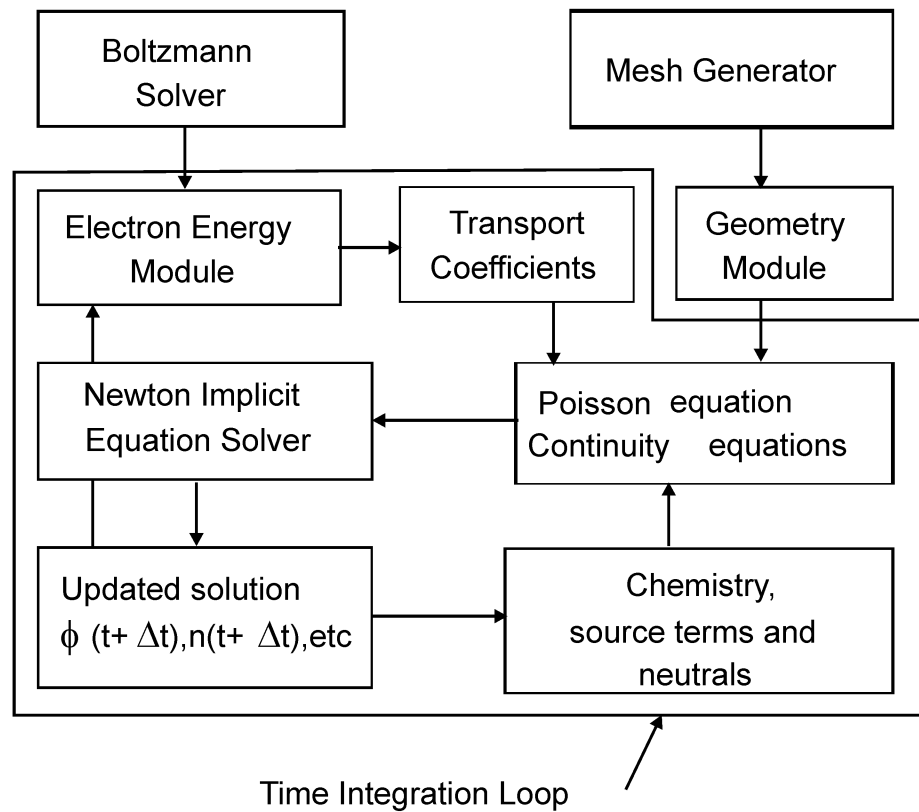


Figure 2.2 Block diagram of the two-dimensional model LAMPSIM.

2.6 References

- ¹ R. Dorai and M. J. Kushner, J. Phys. D: Appl. Phys. **35**, 2594 (2002).
- ² B. M. Lay, R. S. Moss, S. Rauf, and M. J. Kushner, Plasma Sources Sci. Technol. **12**, 8 (2003).
- ³ B. M. Lay, M.S. thesis, University of Illinois at Urbana-Champaign, 2000.
- ⁴ Skyblue Systems Inc., <http://www.skybluesystems.com>

- ⁵ D. L. Scharfetter and H. K. Gummel, IEEE Trans. Electron Dev. **ED-16**, 64 (1969).
- ⁶ SLAP Sparse Matrix Library, <http://www.netlib.org>
- ⁷ M. K. Seager, Lawrence Livermore National Laboratory Technical Report, UCRL-100195 (1998).
- ⁸ M. J. Kushner, J. Appl. Phys. **95**, 846 (2004).

3. INVESTIGATION OF BREAKDOWN IN Ar/Xe MIXTURES

3.1 Introduction

Breakdown in metal halide lamps occurs on time scales of hundreds of nanoseconds to a few microseconds, usually with some starting aid providing background ionization. Measurements for breakdown in Ar/Xe mixtures are available.¹ In those experiments, breakdown times were measured in a lamp geometry closely resembling a commercial metal halide lamp using a Tektronix P5100 probe on a TDS 5104 digital oscilloscope. In this chapter, breakdown modeling efforts are validated by comparing breakdown times predicted using the models to experimental observations. The two-dimensional model enables visualization of the spatial dynamics leading to breakdown.

3.2 Lamp Geometry and Reaction Chemistry

The schematic representation of this lamp used in our computational investigation is shown in Figure 3.1. The lamp is modeled to be cylindrically symmetric about the centerline. The upper electrode is powered while the lower one is grounded. The quartz tube confines the plasma. The largest diameter of the lamp is 5 cm, while the quartz tube has a diameter of 1.0 cm. The interelectrode gap is fixed at 1.6 cm. Dielectric materials separated by air enclose and support the arc tube.

The voltage of the applied pulse is defined as the amplitude to which the pulse approaches asymptotically for the open circuit. A typical experimental voltage waveform is shown in Figure 3.2, which is an applied bias of 2000 V. The voltage across the gap tracks the open circuit voltage when the current is low. When current in the discharge increases voltage dropped across the ballast resistor rises, and the gap voltage falls off

rapidly signifying breakdown of the gas. The pulse repetition frequency for these experiments was 1 Hz. A ballast resistor of 11.5 k Ω is used in series with the lamp. The pulse width lasting a few 1000s of ns is small compared to the interpulse duration of 1 s. There is no significant sustained interpulse electron density, as recombination occurs on much faster timescales after the pulse ends. The effects of any two consecutive voltage pulses can then be assumed to be independent of each other. In the computational study presented here, the effect of a single applied voltage pulse is considered.

The Ar/Xe chemistry considered is listed in Appendix A. The Ar(4s) excited state is denoted as Ar^{*}. Higher excited states (Ar(4p) and others) are lumped together and denoted as Ar^{**}. Three lumped excited states of Xe are included: Xe^{*} (6s states), Xe^{**} (6p states), and Xe^{***} (6s' state). At our pressures of interest, three body collisions are significant, so excited dimer species Ar₂^{*}, Xe₂^{*}, and ArXe^{*} are also included. Charged species include electrons, the singly charged Ar⁺ and Xe⁺, and dimer ions Ar₂⁺, Xe₂⁺, and ArXe⁺ produced by ionization of the corresponding ground/excited states.

3.3 Breakdown Trends using the Zero-Dimensional Model

Trends in mean breakdown times in Ar/Xe mixtures obtained using the zero-dimensional model are presented in this section. The consequences of varying the gas-fill pressure, gas composition, and applied bias will be discussed.

The variation of mean breakdown time with gas-fill pressure for Ar/Xe = 95/5 and 2000 V applied voltage waveform is shown in Figure 3.3. The variation of average electron temperature for these conditions at 10 Torr and 90 Torr is shown in Figure 3.4. Breakdown times predicted by the model for these two cases are 113 ns and 352 ns

respectively. The peak electron temperature at 10 Torr (5.23 eV) is higher than the peak at 90 Torr (3.72 eV). The average electron temperature over the breakdown period is also higher at 10 Torr. The increase in average electron temperature at lower pressures is due to a higher available E/N, and this increases ionization rates, thereby leading to faster breakdown.

The dependence of breakdown time with applied bias is presented in Figure 3.5. The conditions are Ar/Xe = 90/10 at 10 Torr. Larger E/N is available to the discharge at higher voltages, increasing ionization rates and leading to faster breakdown. Experimentally, the effect of voltage on breakdown times is more pronounced at lower voltages. For instance, breakdown time observed experimentally decreases from 900 ns at 800 V to 450 ns at 1000 V. On the other hand, from 1400 V to 2000 V, breakdown time decreases from 250 ns to 180 ns. The model, however, significantly underpredicts breakdown at lower voltages and shows a weak dependence on applied voltage. Breakdown times predicted by the model decreases from 300 ns at 800 V to 120 ns at 2000 V. The electron temperatures calculated for conditions of 90 Torr, 5% Xe and 2000 V and 1500 V, respectively are shown in Figure 3.4. Peak electron temperature decreases from 3.72 eV at 2000 V to 3.6 eV at 1500 V. The average electron temperature is slightly lower at 1500 V and breakdown takes longer.

Breakdown time varies nonmonotonically with gas composition as shown in Figure 3.6. Small fractions of Xe can radically change breakdown times for the mixture. For instance, at conditions of 90 Torr and 2000 V, breakdown time decreases to 352 ns with 5% Xe from 1210 ns with pure Ar. There is little difference as Xe content is varied from 5% to 10%. The minimum breakdown time for this mixture occurs in this

composition interval. Breakdown time increases with Xe content beyond this interval and is calculated to be 842 ns at 40% Xe. The addition of Xe lowers electron temperature as shown in Figure 3.4 corresponding to 5% Xe and 40% Xe, respectively, at 90 Torr and 2000 V. Whereas at small Xe fractions, the decrease in electron temperature is more than compensated by the lower ionization potential of Xe (Xe: 12.3 eV, Ar: 15.78 eV), continued addition of Xe lowers electron temperature further. At 40% Xe for the conditions above, the peak electron temperature is 3.05 eV. The magnitude of drop in electron temperature offsets the advantage of having a lower ionization potential component in the mixture. Similar trends are seen at other pressures and voltages. In general, the consequence of varying composition is more dramatic at higher pressures where breakdown time can decrease by up to a factor of two at small Xe fractions (5-20%).

Breakdown times predicted by the zero-dimensional model capture the general experimental trends. Under certain conditions, deviations become pronounced and the model predictions do not match experimental numbers. For instance, at higher gas pressures or lower applied voltages the deviation from experiment is quite large. The inherent assumption of a uniform electric field in the zero-dimensional model is not representative of actual evolution of discharge parameters, which show propagation delays associated with plasma properties such as electric field, electron density, and electron temperature. At higher pressures and lower voltages, E/N available to the gas rises at a lower rate. Lower voltage rise times and higher pressures mean that E/N available to the gas takes longer to reach the critical value needed to avalanche. Propagation delays would be significant because of lower ionization rates. The discharge

conditions would be markedly nonuniform with regions closer to the powered electrode seeing larger fields than regions further away. In addition, geometric enhancement of electric fields is not accounted for in global modeling and a wider discrepancy can be expected between model and experiment. The closer match to experiments at higher voltages and lower pressures is because higher E/N supplied enhances electron temperature and ionization rates significantly. Propagation delays decrease due to faster ionization and in such conditions, average calculations using the global model provide reasonable estimates.

3.4 Results from the Two-Dimensional Model

In this section, results from two-dimensional dynamic simulations of plasma properties will be discussed. The model lamp is cylindrically symmetric and plasma properties in one-half of the geometry are simulated with appropriate boundary conditions. The base case corresponds to Ar gas-fill at pressure of 30 Torr and applied bias of 2000 V. The voltage pulse is applied at time $t = 0$. Electrons are generated on a continual basis in the gas as a result of universal flux of cosmic rays and the UV source in the experiment. These serve as seed electrons and reduce the statistical lag time component of the breakdown time. An initial uniform electron density 10^6 cm^{-3} corresponding to an ionization fraction of 10^{-12} of the background gas is assumed in the discharge region. The breakdown times predicted by the simulations were compared to experimental data to allow for the parameterization of a volumetric ionization rate of the neutral gas accounting for this background ionization.

3.4.1 Spatial breakdown dynamics

The electron density contours at different time instants leading to breakdown at conditions of the base case are shown in Figure 3.7. Electron density of 10^9 cm^{-3} is produced at regions close to the powered electrode by 75 ns. Electron impact ionization and secondary emission from cathode produce an electron density of 10^7 cm^{-3} near the cathode. In the bulk, electron density starts to increase due to collisional processes. Electron density is spatially inhomogeneous with two distinct regions: ionized regions near the powered electrode with an electron density of 10^9 cm^{-3} , the rest of the discharge having an electron density of $10^5\text{-}10^7 \text{ cm}^{-3}$. The electron avalanche is directed from the powered electrode towards the cathode. By 300 ns, the avalanche has traversed more than half the interelectrode gap. At 355 ns, the avalanche reaches the cathode. The peak electron density is about $1.5 \times 10^{13} \text{ cm}^{-3}$ in regions close to the cathode. The electron density is $10^{11}\text{-}10^{12} \text{ cm}^{-3}$ in the discharge volume close to the axis, where the avalanche is predominant.

The electric potential contours are shown in Figure 3.8. At 50 ns, the potential near the powered electrode and cathode are about 400 V and 10 V, respectively. The electric potential has approximately doubled at locations in the bulk of the discharge by 105 ns. Different regions in the arc tube see different electric field strengths, as the potential field is nonuniform. While regions near the powered electrode are at a potential of 900 V, the potential near the cathode is at 30 V. As ionization of the gas proceeds, potential contour lines are spaced farther apart inside the avalanche, since little voltage is dropped across the conductive plasma. At 300 ns, for instance, the distance along the tube axis of the potential contour lines labeled 1700 V and 1500 V in the ionized regions is

more than eight times that between the 1500 V and 900 V contours. As the avalanche reaches the cathode at 330 ns, the potential drops nearly 1200 V in front of the cathode. As plasma density increases, current through the external circuit rises, leading to a drop in gap voltage. The plasma potential at the center of the arc tube begins to fall. When breakdown is complete at 355 ns, the potential contours recede towards the powered electrode.

The evolution of the magnitude of E/N is shown in Figure 3.9. Initially, E/N is higher in regions close to the powered electrode where the potential is high. By 105 ns, E/N has risen significantly in the discharge volume. The peak in E/N is about 850 Td ($1\text{Td} = 10^{-17} \text{ V}\cdot\text{cm}^{-2}$) near the powered electrode. The region showing comparatively sharper gradients in E/N is the ionization front. The ionization front shifts into the bulk gas from the adjoining areas of the powered electrode at 150 ns. The electric field drops in the conductive plasma behind to 15-30 Td. Compression of the voltage at the leading edge enhances the local electric field. As the front moves, the peak E/N weakens to a magnitude of 500-600 Td and leads the electron avalanche towards the cathode. As the front closes in on the cathode, E/N becomes stronger again and peak values are in the range of 1000-3000 Td ahead of the cathode at breakdown (355 ns).

Electron temperatures are also high at the edge of the ionization front where the electric fields are high (Figure 3.10). For instance, at 150 ns, electron temperatures at the leading edge are 6.0-6.75 eV. In the ionized regions electron temperature falls to about 3.5-4.0 eV, which sustains the high plasma density. High electron temperatures at the leading edge of the front increase rates of electron impact ionization. The peak magnitude of the sources (Figure 3.11) is $5 \times 10^{19} \text{ cm}^{-3}$ at 250 ns. There are gradients on either side of

the ionization front as the peak in source terms moves with it. Behind the front, the magnitude of source terms falls to 10^{16} - 10^{17} $\text{cm}^{-3}\text{s}^{-1}$ in the ionized regions. Ahead of the front, source terms are higher due to seeding by photoionization. The magnitude of sources gradually falls from 10^{16} cm^{-3} to 10^{12} - 10^{13} cm^{-3} towards the grounded electrode. By 316 ns, the peak in the sources is just ahead of the cathode and electron temperatures (8.5-9.0 eV) increase peak source terms to 10^{21} $\text{cm}^{-3}\text{s}^{-1}$. Large source terms are sustained in this region through breakdown and potential contours start retreating at this point. Source terms increase along the axis as E/N recovers to 60-80 Td and electron temperatures increase to 4-4.2 eV (340 ns). At 355 ns, source terms in these locations are 10^{18} - 10^{19} $\text{cm}^{-3}\text{s}^{-1}$.

The rate of production of Ar_2^+ from Ar^+ is 10^6 s^{-1} at 30 Torr and hence Ar^+ is the dominant ion in the plasma on the breakdown timescales. During the avalanche process, the density of Ar^+ ahead of the avalanche is 10^7 - 10^8 cm^{-3} and 10^{11} cm^{-3} in the avalanche. When the avalanche closes the gap, ion density near the cathode peaks at 5×10^{12} cm^{-3} and is about 10^{11} - 10^{12} cm^{-3} along the axis of the arc tube. Ion density away from the axis and close to the walls is 10^7 - 10^8 cm^{-3} . Electron density is low, about 10^6 cm^{-3} . Higher electron mobility results in negative charging of the walls and a positive space charge region develops close to the walls. The charging process is rapid and by 50 ns walls are negatively charged to 10^6 - 10^7 cm^{-3} . The ionization front itself is characterized by positive space charge and the local electric field is enhanced in regions of the front within a small distance from the axis. The close positioning of the peak in the electric field magnitude to the axis ensures that the ionization front moves close to the axis and towards the cathode.

The dynamics of the secondary electron source terms near the cathode are shown in Figure 3.12. At 105 ns, photoemission from the cathode comprises the major fraction of secondary electron sources (10^{14} - 10^{16} cm^{-3}). The ion density near the powered electrode is 10^{11} cm^{-3} at this point; however, the ion transit time to the grounded electrode is large. The ion flux to the cathode is mainly from regions surrounding the cathode. This flux is low because of small ion densities (10^8 cm^{-3}) here. Ion bombardment of the cathode is the minor component for secondary emission in the early stages of breakdown. Secondary sources have not increased significantly until 300 ns, when the ionization front approaches close to the cathode.

Ion density behind the leading edge of the ionization front is about 10^{11} cm^{-3} . The ion flux increases with the approach of the ionization front after 300 ns, leading to the emission of secondary electrons from the cathode surface. These beam electrons are energetic and travel a considerable distance from the cathode surface into the gas. In their path, they create further electrons by way of electron impact ionization of the neutral gas species (335 ns). Ions thus created are accelerated by the high electric fields and create more secondary electrons by bombarding the cathode. The feedback ensures a significant increase in secondary electron sources near the cathode. The dramatic increase in secondary sources is shown in Figure 3.12. The increase is about three orders of magnitude as the avalanche front strikes the cathode. Peak secondary emission sources rise to 10^{19} cm^{-3} at 355 ns compared to 10^{16} cm^{-3} at 300 ns before the arrival of the avalanche. At this time, ion bombardment (10^{17} - 10^{19} cm^{-3}) has replaced photoelectric emission (10^{14} - 10^{16} cm^{-3}) as the principal means of secondary electron production. It is

expected that ion bombardment will continue to be the principal means of secondary emission in the glow phase as well, as the discharge becomes self-sustaining.

Secondary emission plays a vital role in propagating the ionization front to establish gap closure. In the absence of photoemission, the propagating ionization front ‘stuck’ at the center of the discharge and gap closure was not observed in the simulations. This is corroborated by experiments where breakdown was at best inconsistent in the absence of the UV source. Once the discharge is self-sustaining, however, the removal of the photoemission source is not expected to affect its evolution.

3.4.2 Effect of varying composition

In this section, compositional effects of Xenon on the breakdown dynamics in Ar/Xe mixtures will be discussed. Trends in breakdown time are shown in Figure 3.13. In an Ar/Xe mixture consisting of 10% Xe, breakdown occurs at 275 ns. Plasma properties at this instant are shown for comparison with the dynamics of the base case Ar gas-fill in Figures 3.14 and 3.15. While electrons have completely avalanched the interelectrode gap in the Ar/Xe mixture, the avalanche has covered just half this distance in Ar. The higher speed of the ionization front in the mixture compared to the Ar gas-fill is because the net rate of electron generation is higher in the mixture. When compared to the base case, E/N along the ionization front is reduced from 500-600 Td to 400-500 Td (Figure 3.16).

The addition of Xe lowers peak electron temperatures. For Ar/Xe=90/10, T_e varies between 5.0 and 6.0 eV at the ionization front (Figure 3.17). In the ionized regions, electron temperatures are 2.6-3.0 eV. With Ar/Xe=40/60 the electron temperature is lower in the ionized regions (2.3-2.6 eV). Peak electron temperatures are 4.6-4.9 eV at

the ionization front (Figure 3.17). Higher momentum transfer losses shift electron energy distribution towards lower energies. The lower electron temperature at the ionization front with Ar/Xe=40/60 results in the slower movement of the avalanche (Figure 3.14) and increases breakdown time.

With Ar/Xe=90/10, the ratio of Xe^+/Ar^+ densities is 1.0-2.0 ahead of the propagating front where E/N is 100-200 Td and electron temperature is 4.0-4.5 eV. In regions with E/N of 250-500 Td and electron temperatures of 5.0-6.0 eV, however, Ar^+ is the dominant ion as a result of increased ionization. The dominant ion in the ionized regions is Xe^+ (Figure 3.18), the ratio of Xe^+/Ar^+ densities going up to 3.0. Xe has a lower ionization potential compared to Ar (Xe: 12.13 eV, Ar: 15.78 eV). The cross section of ionization of Xe is higher than that of Ar. It is therefore expected that Xe be preferentially ionized over Ar. With Ar/Xe=40/60, Xe^+ is the dominant ion throughout the discharge, since Xe comprises the major fraction and its ionization energy is lower.

Density of species Ar^{**} are shown in Figure 3.19 for three cases of pure Ar, 10% Xe, and 60% Xe at 275 ns. With Ar/Xe=90/10, the density of Ar^{**} is comparable to Ar^+ ($10^{11} cm^{-3}$) in the ionized regions. The rate of Penning ionization of Xe atoms by Ar metastables is $10^{18} cm^3 s^{-1}$ here, and is a major source of electron generation. Ar^{**} density behind the front remains high (10^{10} - $10^{11} cm^3$) and Penning ionization rates in these ionized regions are sustained through breakdown (10^{17} - $10^{18} cm^3 s^{-1}$). Lower electron temperatures and the lower Ar fraction explain the decrease in Ar^+ density to 2×10^{10} - $5 \times 10^{10} cm^{-3}$ at 60% Xe (from 1×10^{11} - $5 \times 10^{11} cm^{-3}$ at 10% Xe) in the ionized regions. Peak Ar^{**} density ($\sim 10^{10} cm^{-3}$) moves along with the ionization front and falls off on either side ($\sim 10^7$ - $10^8 cm^{-3}$). Since the excited states of Xe have lower thresholds (Xe*: 8.36 eV,

Xe^{**}: 9.73 eV) compared to those of Ar (Ar^{*}: 11.6 eV, Ar^{**}: 13.3 eV) and electron temperatures are reduced, Ar^{*} and Ar^{**} production rates decrease in the ionized regions. Rates of Penning ionization of Xe by Ar^{**} therefore peak in the ionization front (10^{18} cm³s⁻¹) and fall off on either side (10^{14} - 10^{15} cm³s⁻¹), similar to the contours of Ar^{**} (Figure 3.19). Xe⁺ densities in the ionized regions do not show significant differences compared to 10% Xe case ($\sim 10^{11}$ cm⁻³) as increased ionization from the ground and excited states compensates for the decrease in Penning ionization rates.

Trends in mean breakdown time with Xe composition calculated using this model are shown in Figure 3.13. At 70 Torr, 2000 V applied bias, the breakdown time decreases from 877 ns for pure Ar fill to around 475 ns with 10% Xe. In all cases, breakdown times initially decrease as the fraction of Xe increases to 10%. Minimum breakdown times are seen in the 5-20% Xe fraction window across a wide range of pressures and applied voltage conditions. Beyond this window, mean breakdown times increase with Xe content. Breakdown is not necessarily observed for all sets of pressure, composition, and applied voltages. For instance, no breakdown is observed at a Xe fraction of 0.8 and beyond at 90 Torr and 2000 V. The avalanche cannot be maintained, as the decrease in electron energy wrought by momentum transfer losses is not adequately compensated by the applied E/N.

3.4.3 Effect of varying pressure

The effect of pressure on breakdown dynamics is less dramatic. Discharge properties are shown for Ar at 70 Torr in Figures 3.14 and 3.15. While E/N at the ionization front in the base case is 600-650 Td (Figure 3.16), it decreases to 300-420 Td

at 70 Torr. Peak electron temperatures are also lower at 70 Torr (4.5-5.5 eV) as shown in Figure 3.17. The ionization rate coefficient of Ar with applied E/N is shown in Figure 3.20 and varies from 5×10^{-9} - $10^{-8} \text{ cm}^3 \text{ s}^{-1}$ to 10^{-10} - $10^{-9} \text{ cm}^3 \text{ s}^{-1}$ as E/N is decreased from 600-650 Td to 100-300 Td. Lower electric fields and electron temperatures decrease the rate of electron avalanche due to reduction in ionization rates. The peak in source terms is $2.0 \times 10^{19} \text{ cm}^{-3} \text{ s}^{-1}$ and the average magnitude of sources at the ionization front is lower compared to the base case. Consequently, the movement of the ionization front is slower at 70 Torr. In the range of pressures considered for this study (10-50 Torr), breakdown times increased with pressures for various conditions of composition and applied voltage as shown in Figure 3.21.

3.4.4 Effect of varying applied bias

The dynamics of breakdown do not change much at lower applied bias. To determine the effect on spatial dynamics, conditions of Ar, 30 Torr and 1500 V were simulated and compared to the base case discharge properties. The peak E/N at ionization front is 600 Td at the lower applied bias and weakens to about 500 Td as the front progresses. Lower bias increases the delay before the critical E/N required for electron avalanche forms, since the voltage rise time increases. E/N in the bulk gas ahead of the ionization front is lower at 1500 V (10-30 Td) compared to 2000 V (50-100 Td), leading to electron impact sources (10^{10} - $10^{11} \text{ cm}^3 \text{ s}^{-1}$) that are two orders of magnitude lower than at 2000 V. Both these factors decrease the rate of electron avalanche towards the cathode at 1500 V.

The dependence of mean breakdown time with applied voltage is shown in Figure 3.22 for various discharge conditions. As applied voltage increases from 800 V to 1000 V at 10 Torr, breakdown time falls from 798 ns to 494 ns. The decrease, however, is asymptotic and beyond an applied voltage of 1800 V breakdown times does not change significantly. The ionization rate coefficient of Ar (Figure 3.20) begins to saturate at E/N beyond 1000 Td ($\sim 10^{-8} \text{cm}^3 \text{s}^{-1}$). Further increase in the applied E/N will not result in significant increase in electron sources and the speed of the ionization front approaches an asymptotic value.

3.5 Concluding Remarks

Zero-dimensional and two-dimensional modeling studies of the breakdown process in Ar/Xe mixtures based on an experimental lamp geometry are reported. Modeling predictions of breakdown times were compared to experimental data. The zero-dimensional model gives reasonable agreement of experimental trends. However, it does underpredict breakdown times over a range of compositions and pressures. This is because of propagation delays in plasma parameters, such as electric field and electron density, which are far from being spatially homogeneous under these conditions on breakdown time scales.

The two-dimensional model is able to capture the spatial dynamics involved in breakdown. Simulations of plasma properties show a Townsend-like propagation of the ionization front leading to breakdown. Secondary electron emission is vital to the closure of the interelectrode gap and is dominated here in large part by photoemission in the early

stages of breakdown. Ion bombardment dominates secondary sources towards the end of the breakdown process.

Parameterizations were performed validating the two-dimensional model with experimental data. Lower applied voltages increase breakdown times by delaying the critical E/N needed to avalanche the gas. Ionization rates are decreased at higher pressures due to lower electron temperatures resulting from lower E/N . Small fractions of Xe (5-10%) are beneficial in decreasing breakdown times by providing a low ionization energy component for electron impact ionization and by Penning ionization. Larger Xe fractions increase momentum transfer losses decreasing the electron temperature at the ionization front, leading to lower ionization rates and longer breakdown times.

3.6 Figures

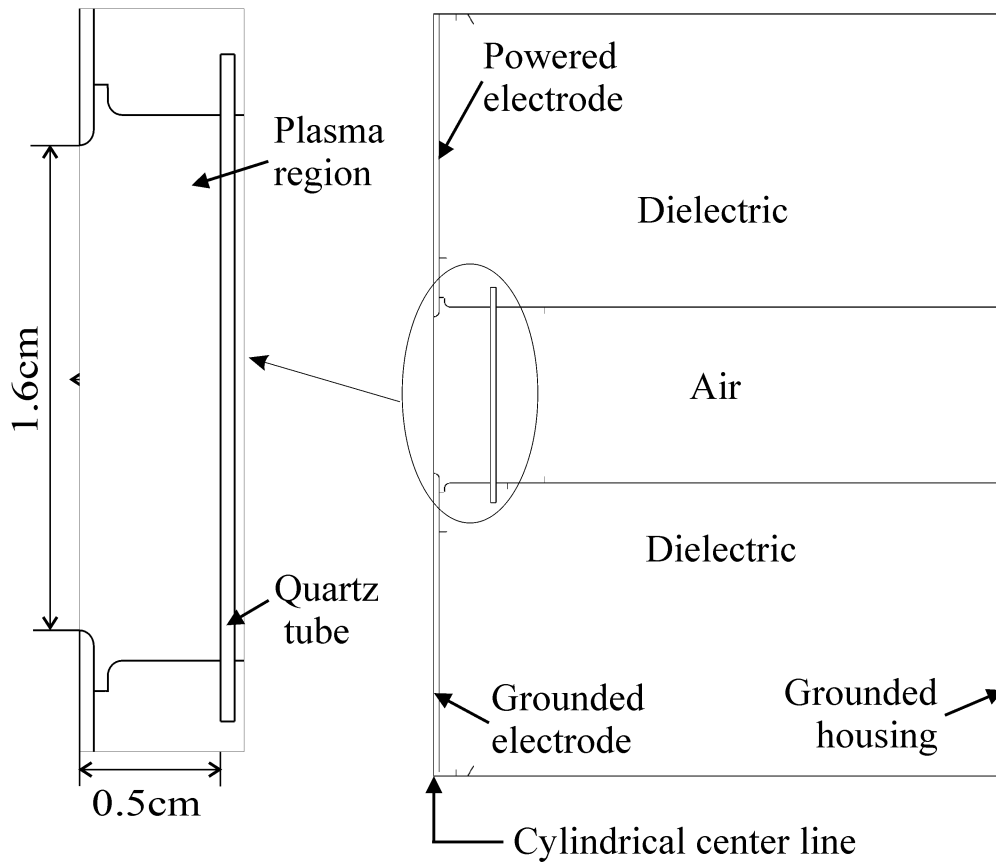


Figure 3.1 Schematic of the lamp geometry. The lamp is modeled to be cylindrically symmetric. The quartz tube (shown on the left) has a radius of 0.5 cm with an interelectrode gap of 1.6 cm.

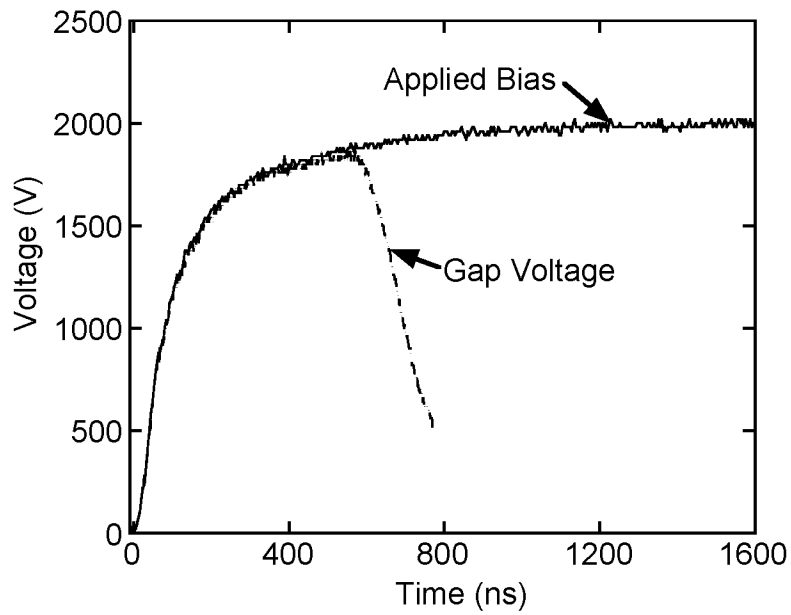


Figure 3.2 The experimental 2000 V waveform. Gap voltage falls off when breakdown occurs.

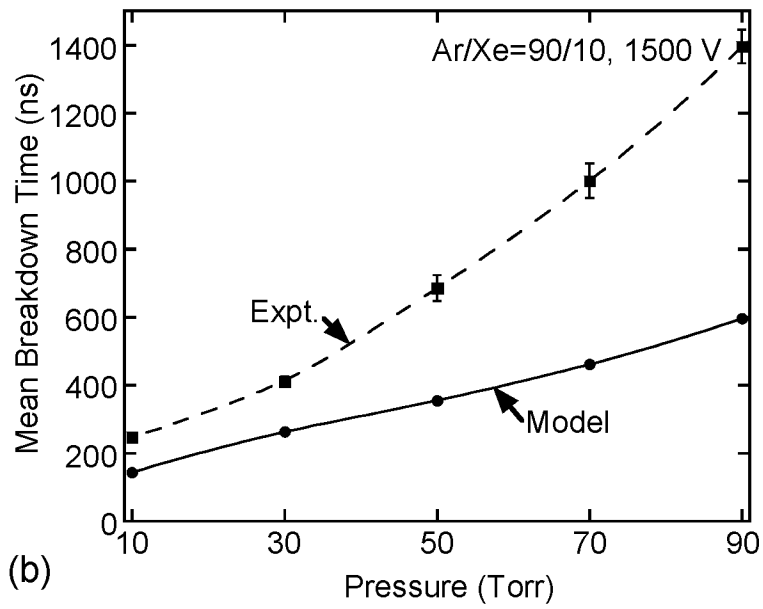
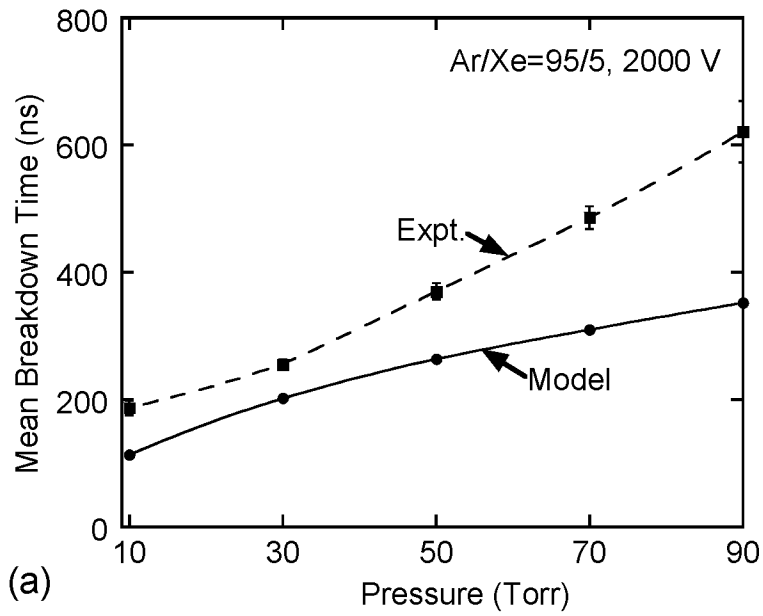


Figure 3.3 Effect of pressure of gas-fill on the breakdown times predicted using the zero-dimensional model for (a) Ar/Xe=95/5, 2000 V and (b) Ar/Xe=90/10, 1500 V.

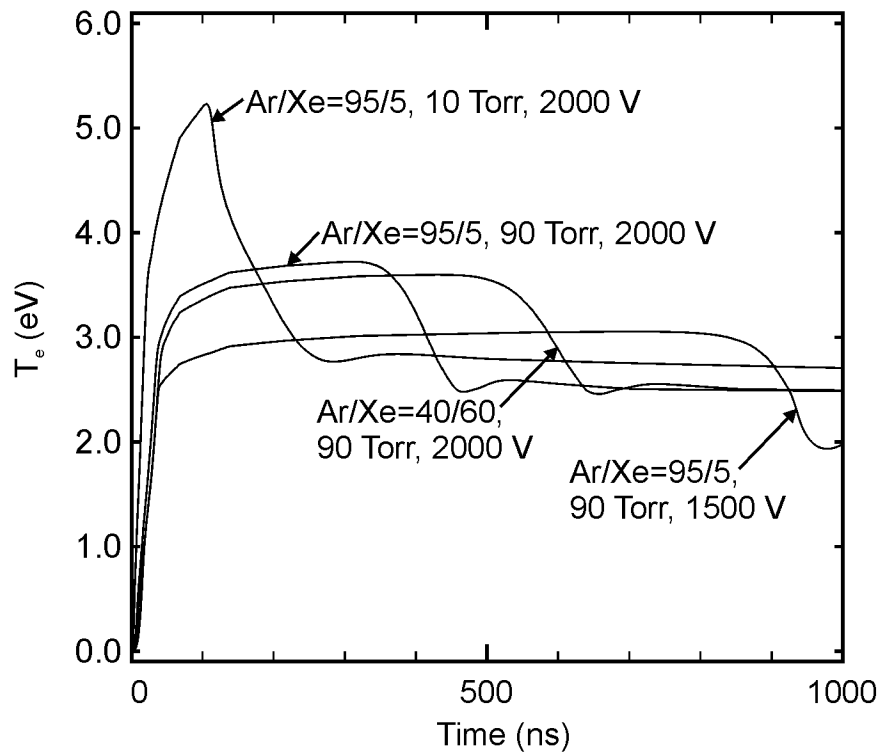
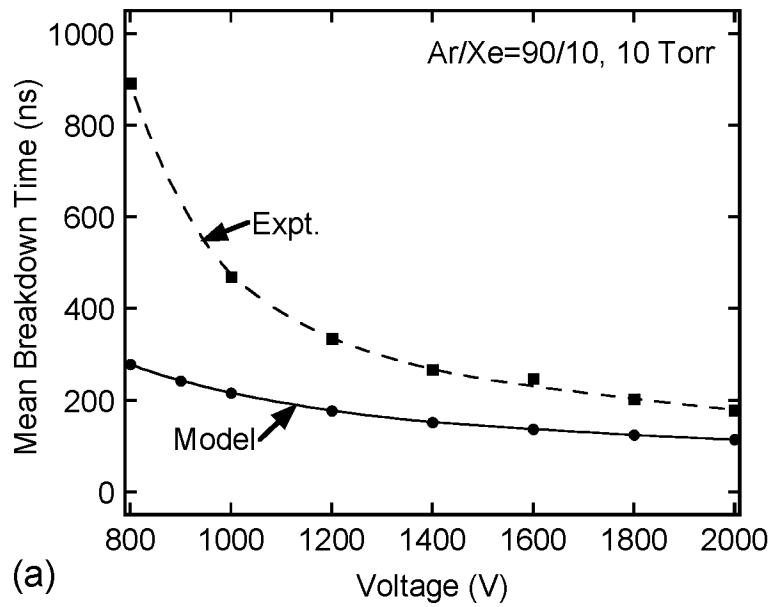
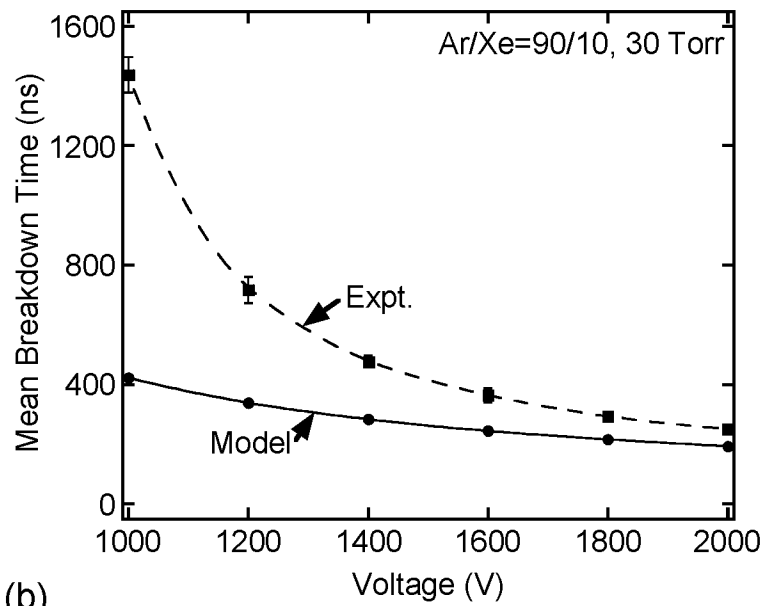


Figure 3.4 Variation of electron temperature with time predicted with the zero-dimensional model for different conditions.



(a)



(b)

Figure 3.5 Effect of applied bias on the breakdown times predicted using the zero-dimensional model for (a) Ar/Xe=90/10, 10 Torr and (b) Ar/Xe=90/10, 30 Torr.

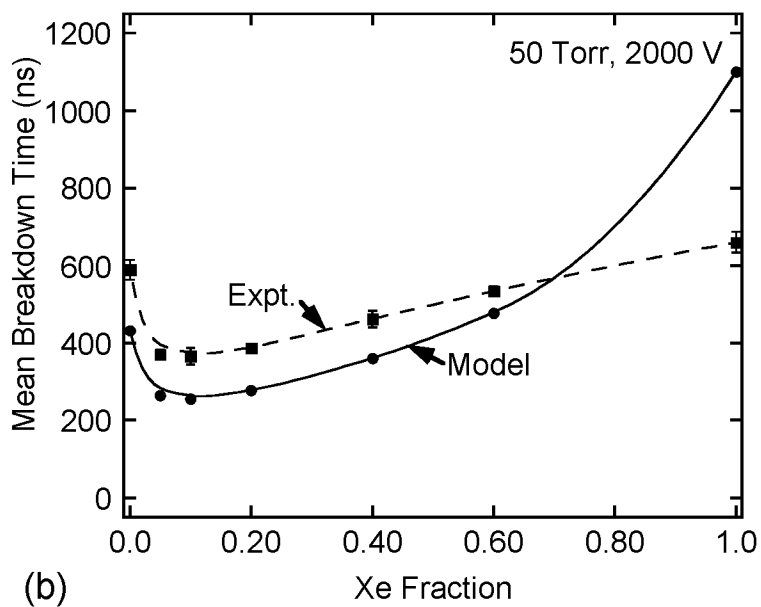
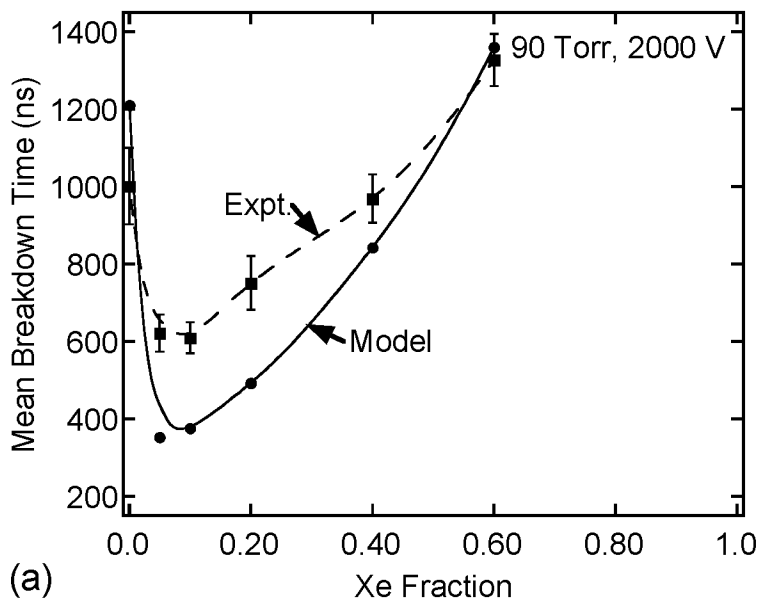


Figure 3.6 Effect of composition of Ar/Xe mixture on the breakdown times predicted using the zero-dimensional model for (a) 90 Torr, 2000 V and (b) 50 Torr, 2000 V.

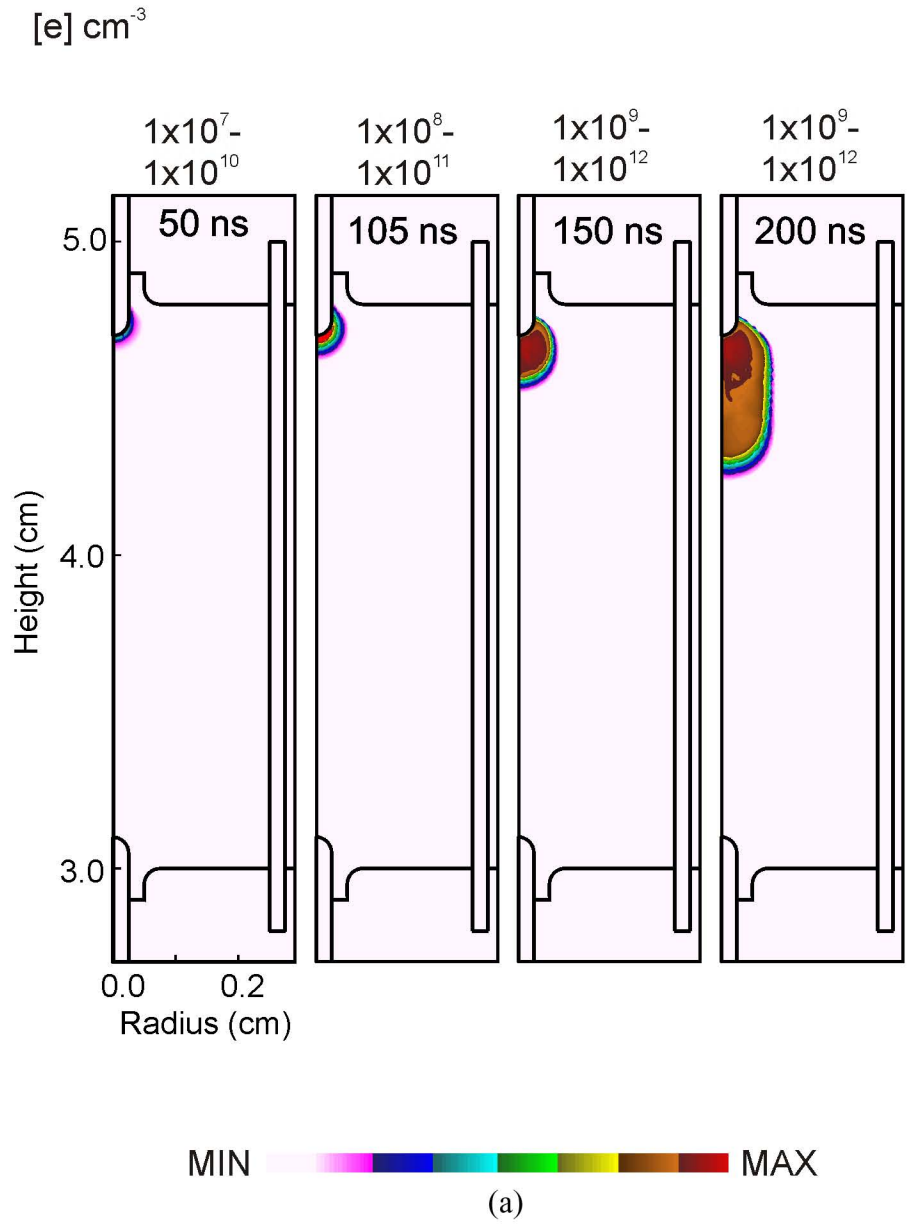
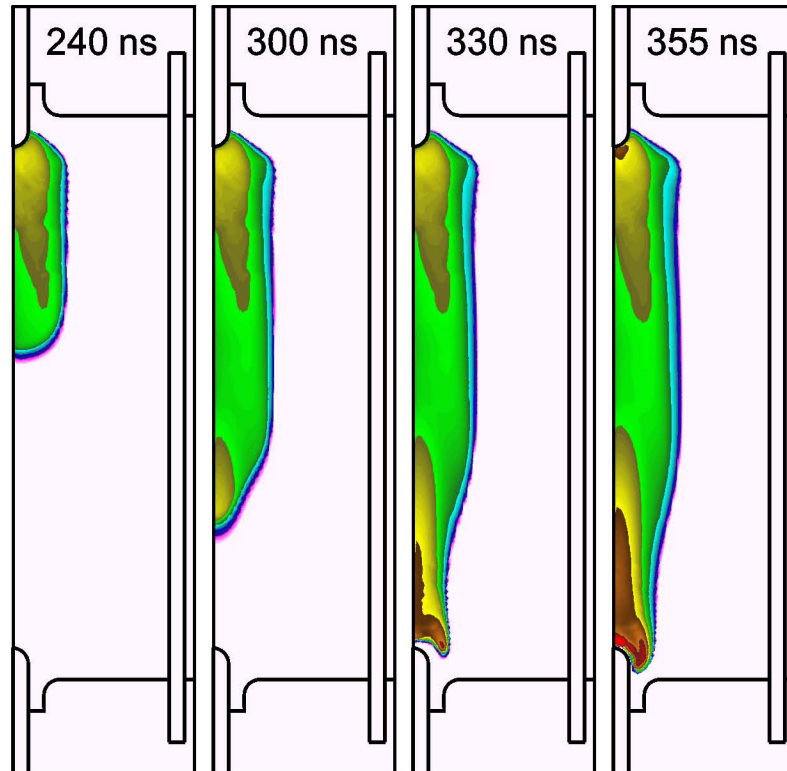


Figure 3.7 (a) Electron density (log scale, cm⁻³) at different instants of time during breakdown for the base case (Ar, 30 Torr, 2000 V). (b) Breakdown occurs at 355 ns.

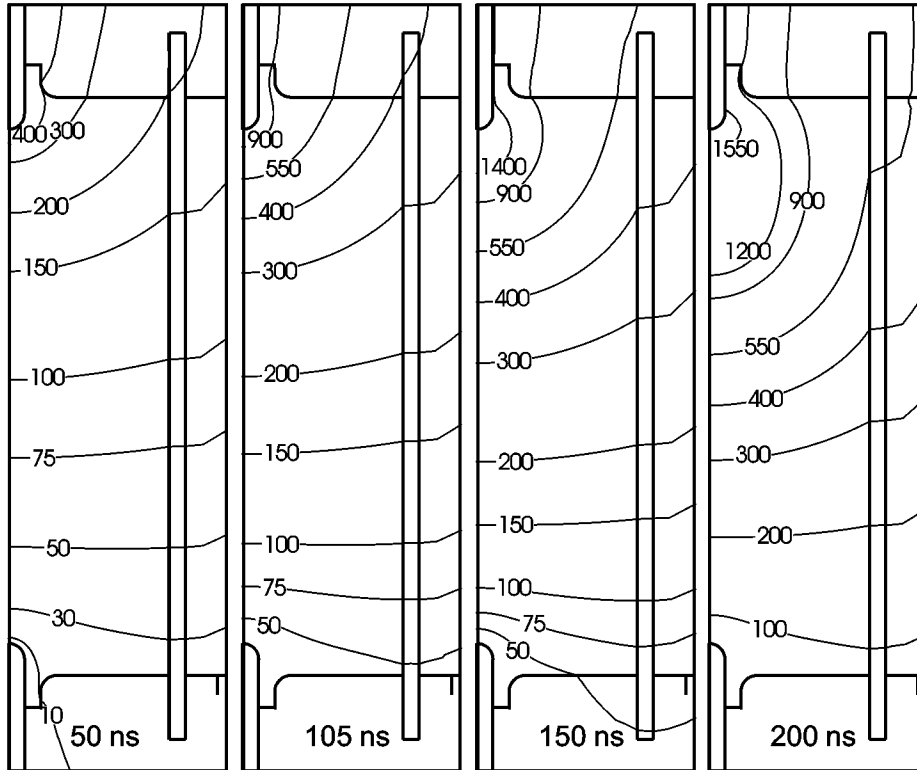
[e] cm⁻³



(b)

Figure 3.7, cont.

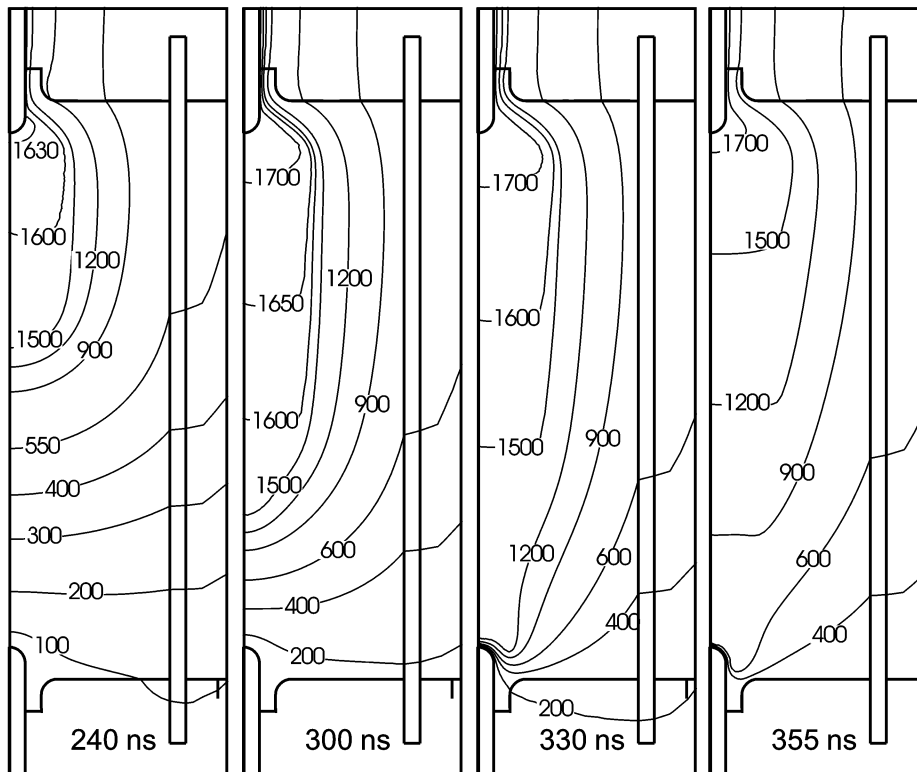
Potential (Volts)



(a)

Figure 3.8 (a) Electric potential contours at different instants leading to breakdown for the base case conditions (Ar 30 Torr, 2000 V). (b) The larger conductivity of the ionized regions is evident as the potential contours as compressed ahead of the ionization front.

Potential (Volts)



(b)

Figure 3.8, cont.

E/N (V-cm²)

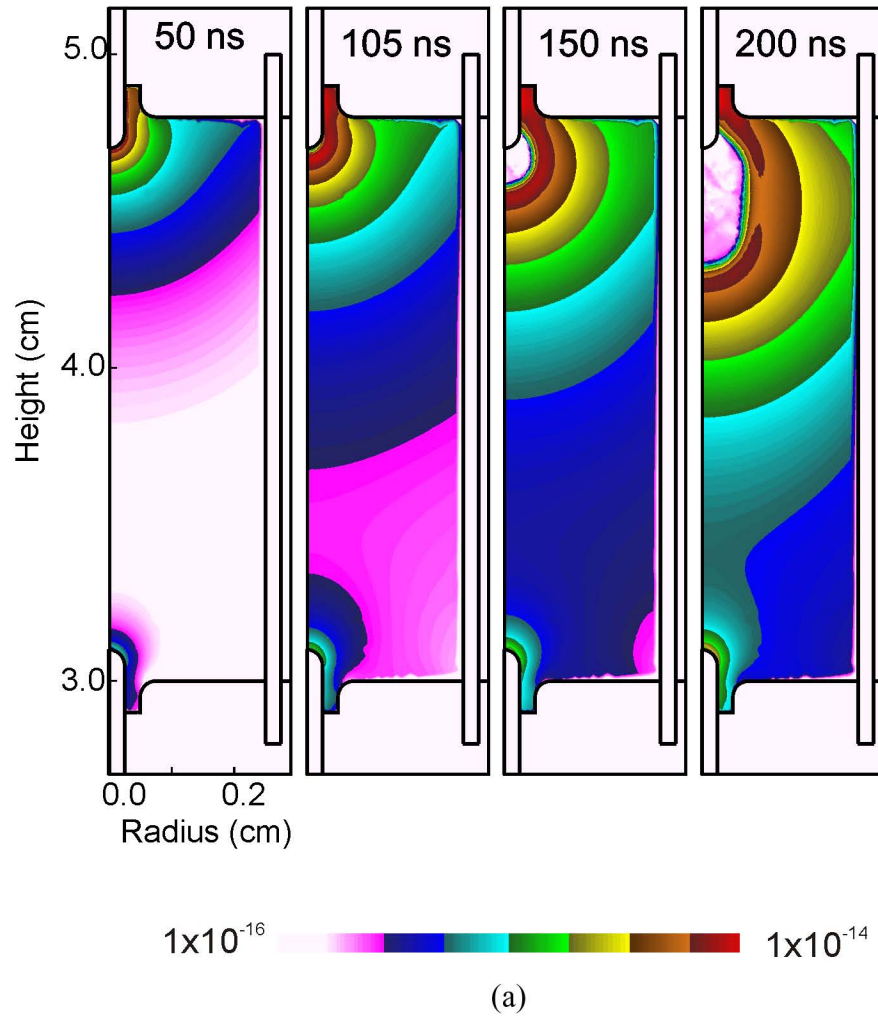
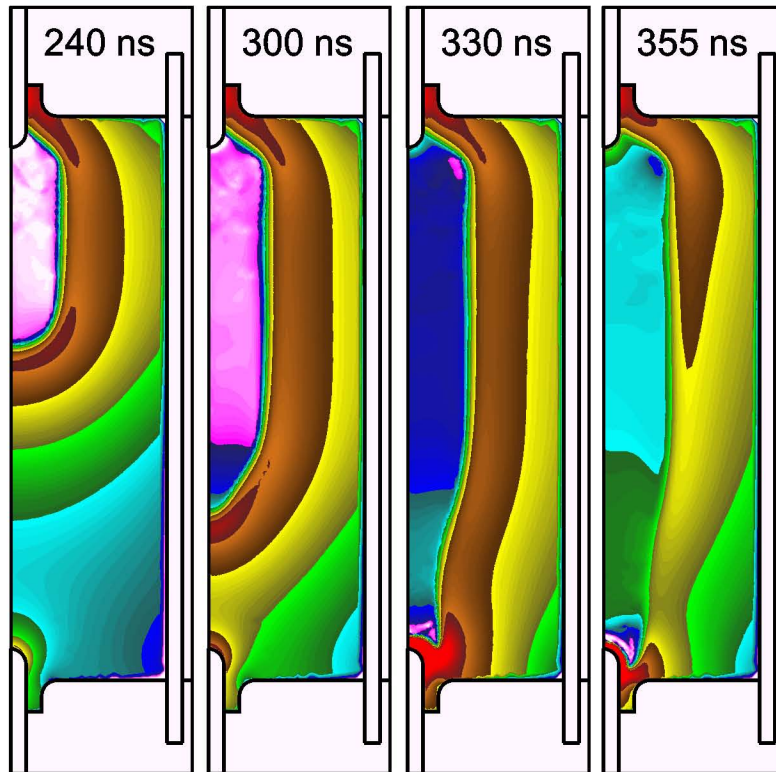



Figure 3.9 (a) The magnitude of E/N (log scale, V-cm²) is shown at different times during the breakdown event for the base case conditions (Ar 30 Torr, 2000 V). (b) Steep gradients in E/N indicate the position of the ionization front.

E/N (V-cm²)



1x10⁻¹⁶  1x10⁻¹⁴

(b)

Figure 3.9, cont.

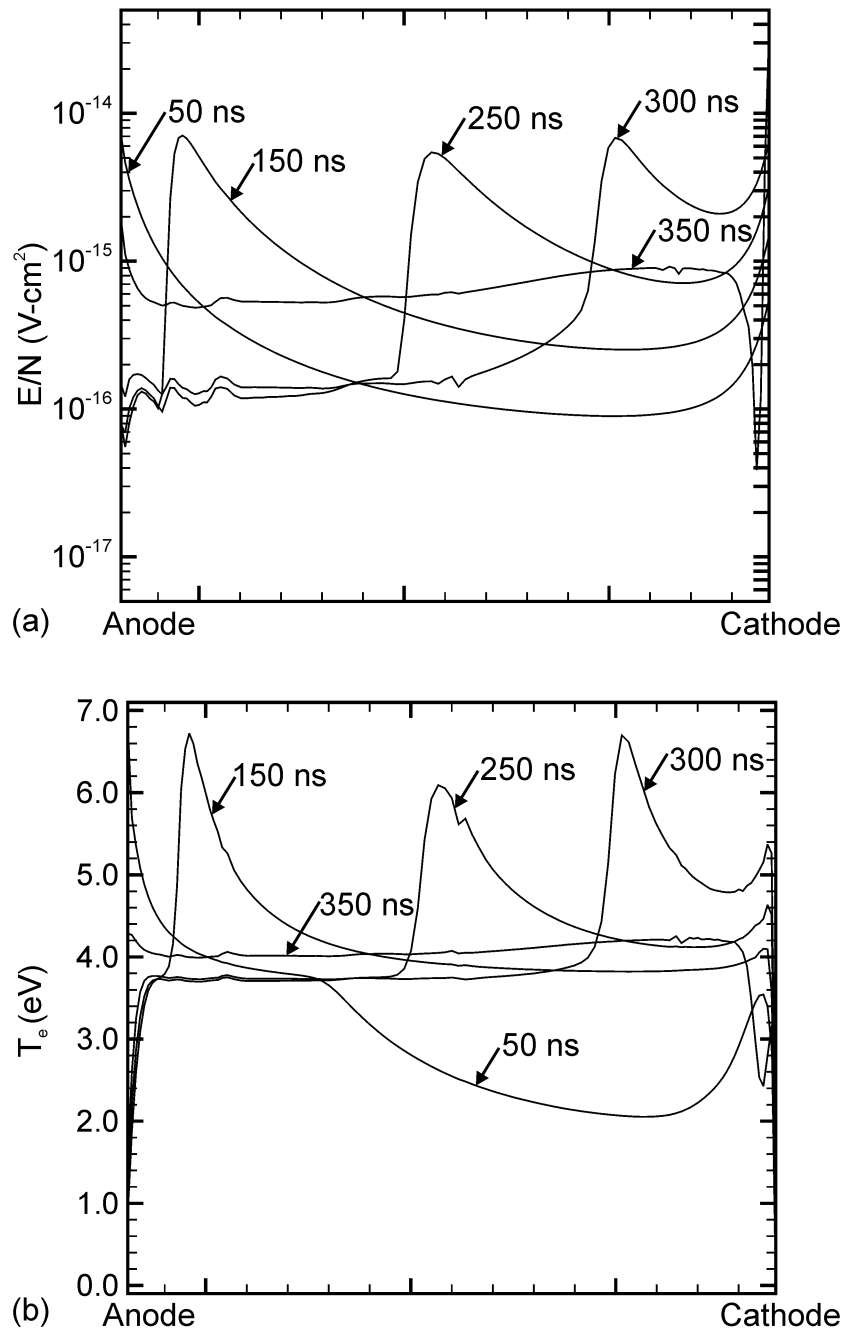
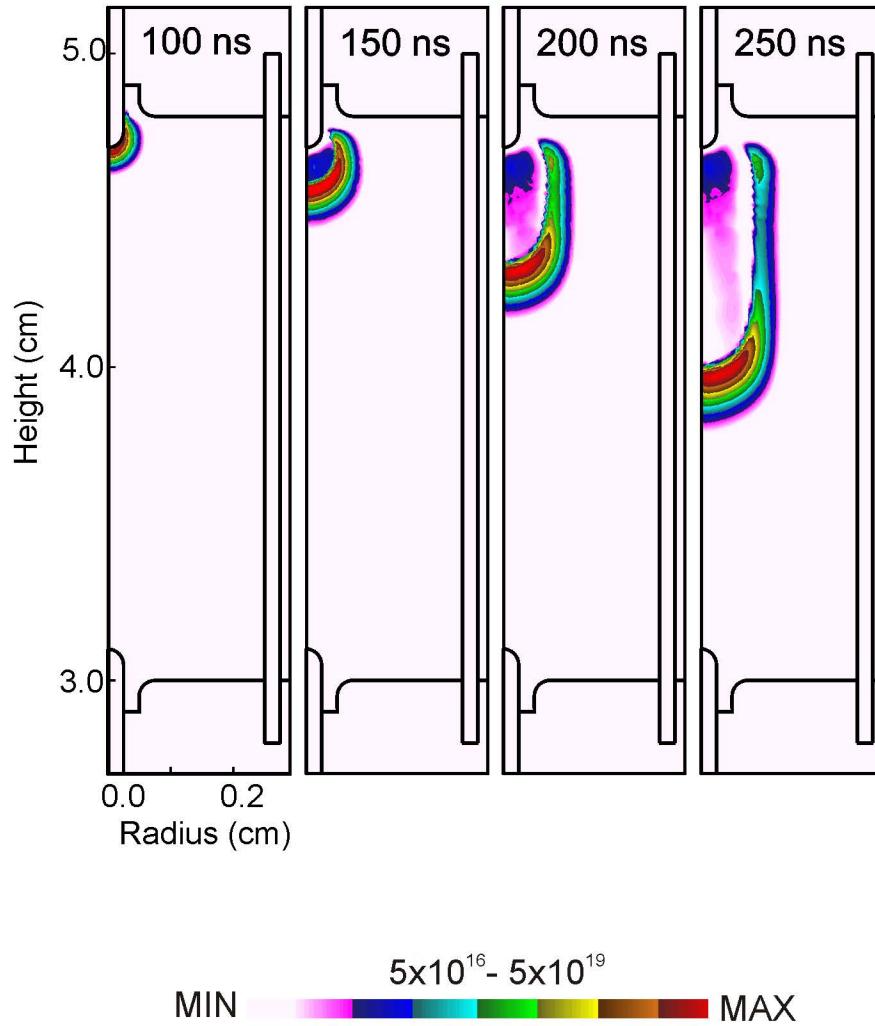


Figure 3.10 The variation of plasma parameters (a) E/N and (b) T_e is shown at locations on the axis of the arc tube for base case conditions (Ar 30 Torr, 2000 V).

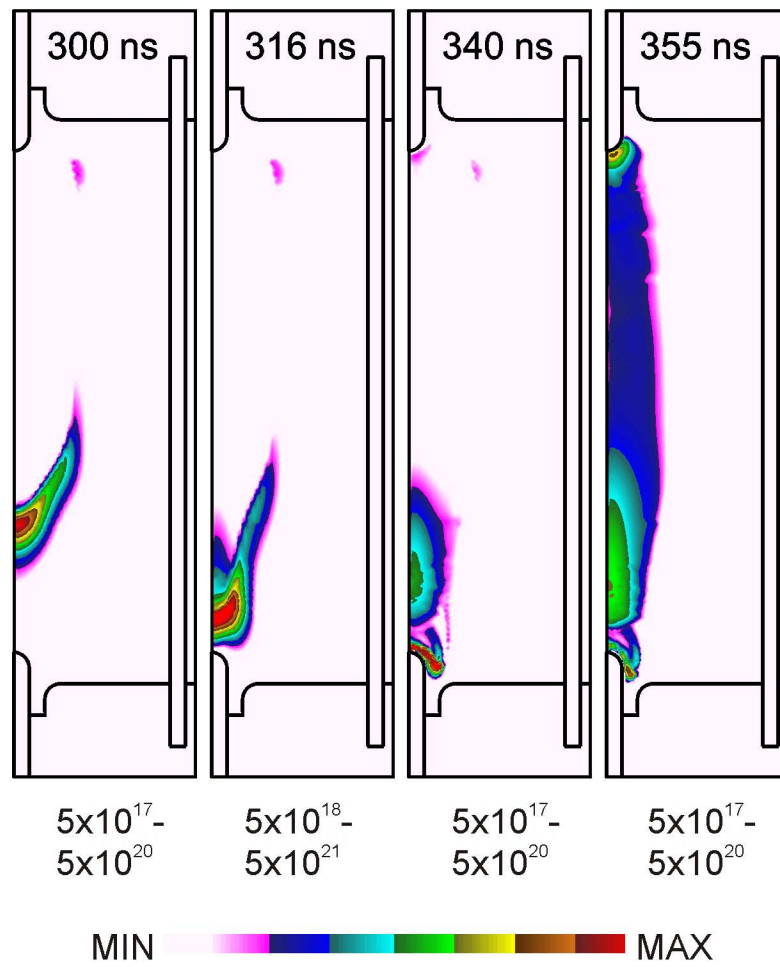
$S_e(\text{cm}^{-3}\text{s}^{-1})$



(a)

Figure 3.11 (a) Electron impact sources (log scale, $\text{cm}^{-3}\text{s}^{-1}$) are shown at different times for the base case conditions (Ar 30 Torr, 2000 V). (b) The peak in electron sources tracks the peak in E/N as it moves across the interelectrode gap.

$S_e(\text{cm}^{-3}\text{s}^{-1})$



(b)

Figure 3.11, cont.

S-ionization $\text{cm}^{-3}\text{s}^{-1}$

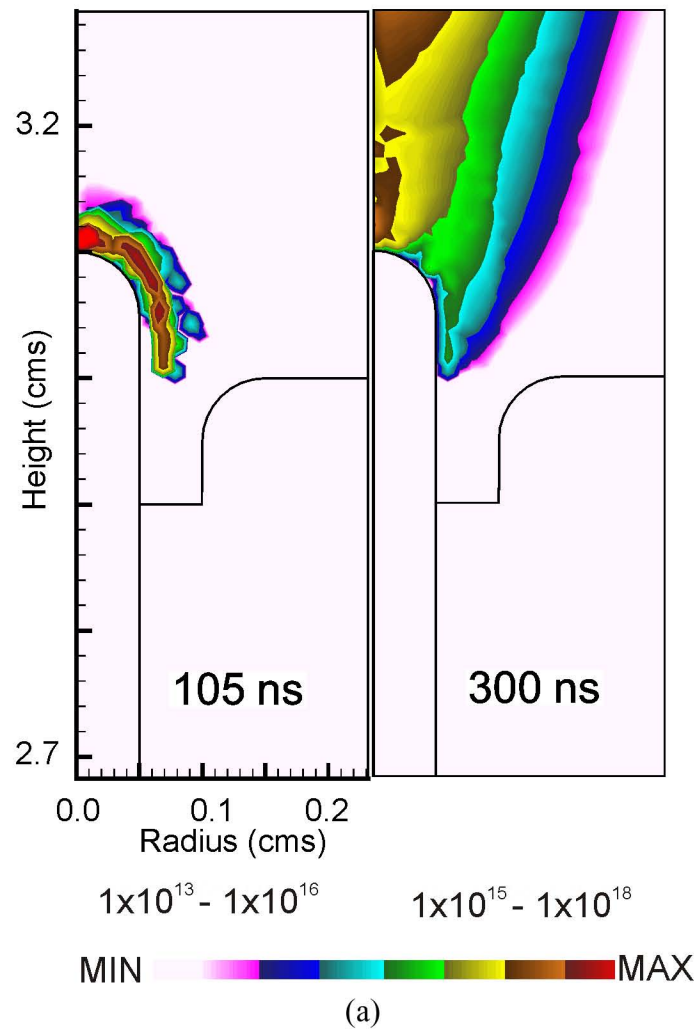
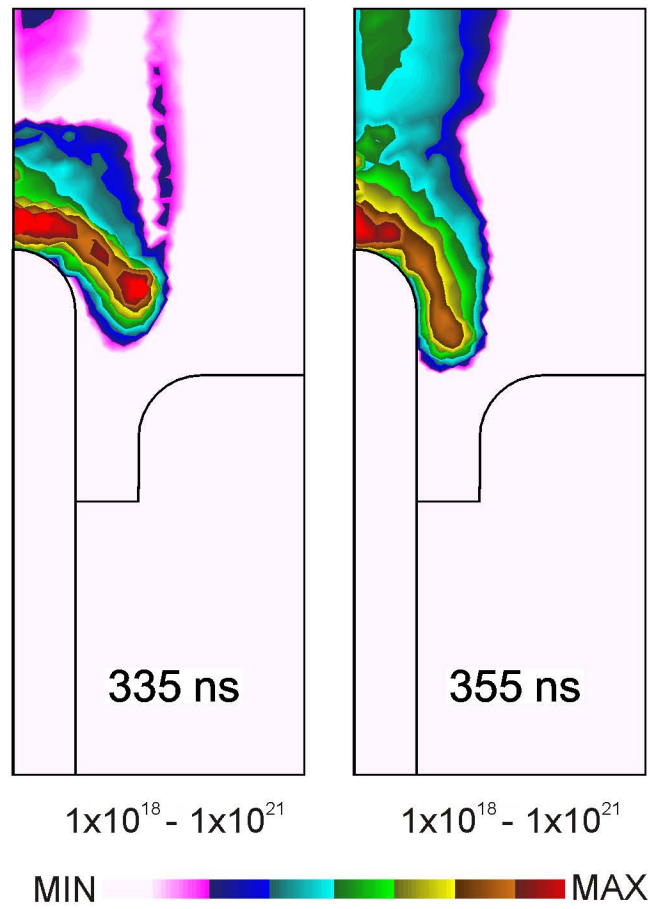


Figure 3.12 (a) Ionization sources near the cathode (log scale, $\text{cm}^{-3}\text{s}^{-1}$) at different times during the breakdown event for the base case (Ar 30 Torr, 2000 V). (b) Ionization sources near the cathode increase rapidly as the ionization front closes in, due to ion bombardment.

S-ionization $\text{cm}^{-3}\text{s}^{-1}$



(b)

Figure 3.12, cont.

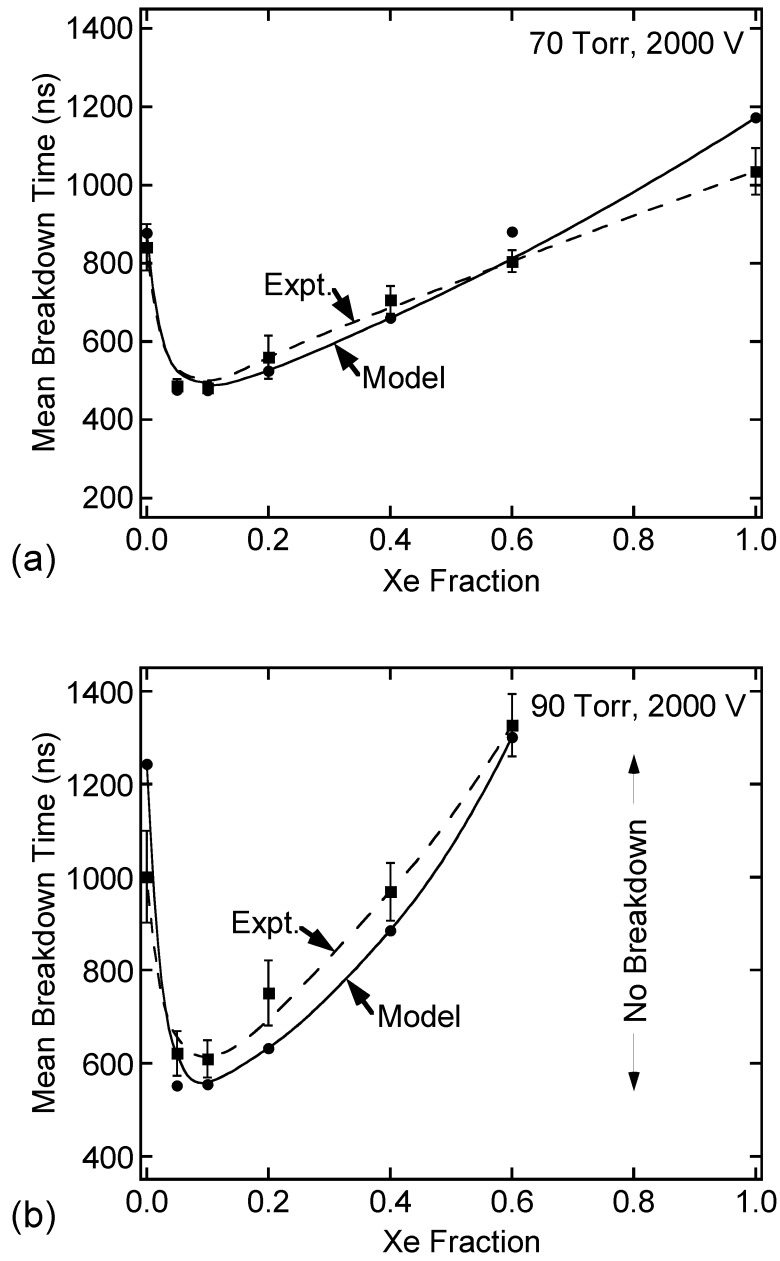
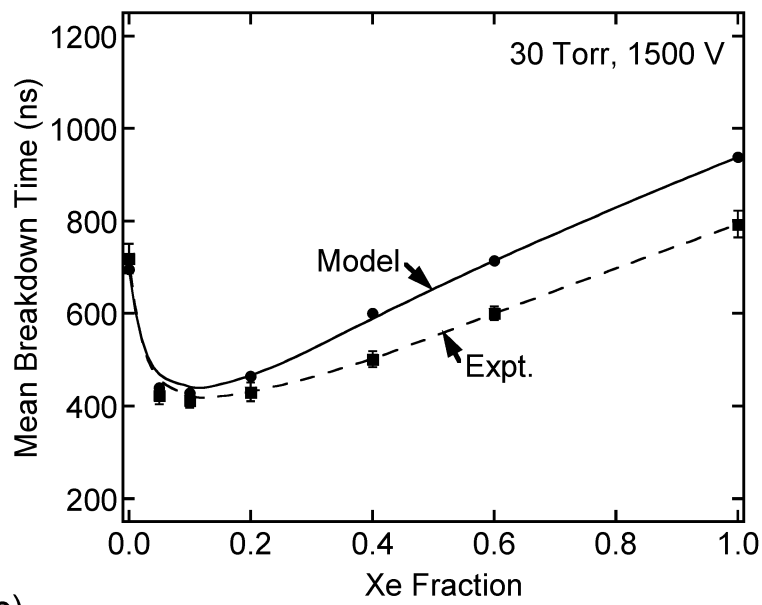


Figure 3.13 Effect of composition on the breakdown times in Ar/Xe mixtures using the two-dimensional model for (a) 70 Torr, 2000 V, (b) 90 Torr, 2000 V and (c) 30 Torr, 1500 V.



(c)

Figure 3.13, cont.

[e] cm⁻³

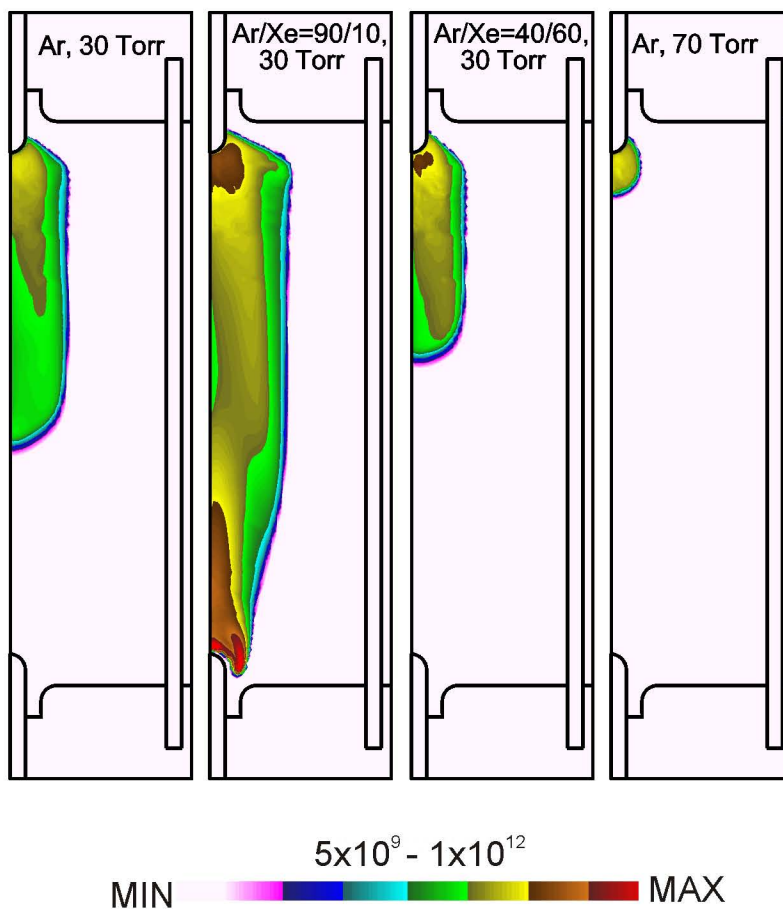


Figure 3.14 Electron density (log scale, cm⁻³) at 275 ns for different compositions and pressures.

S-ionization $\text{cm}^{-3}\text{s}^{-1}$

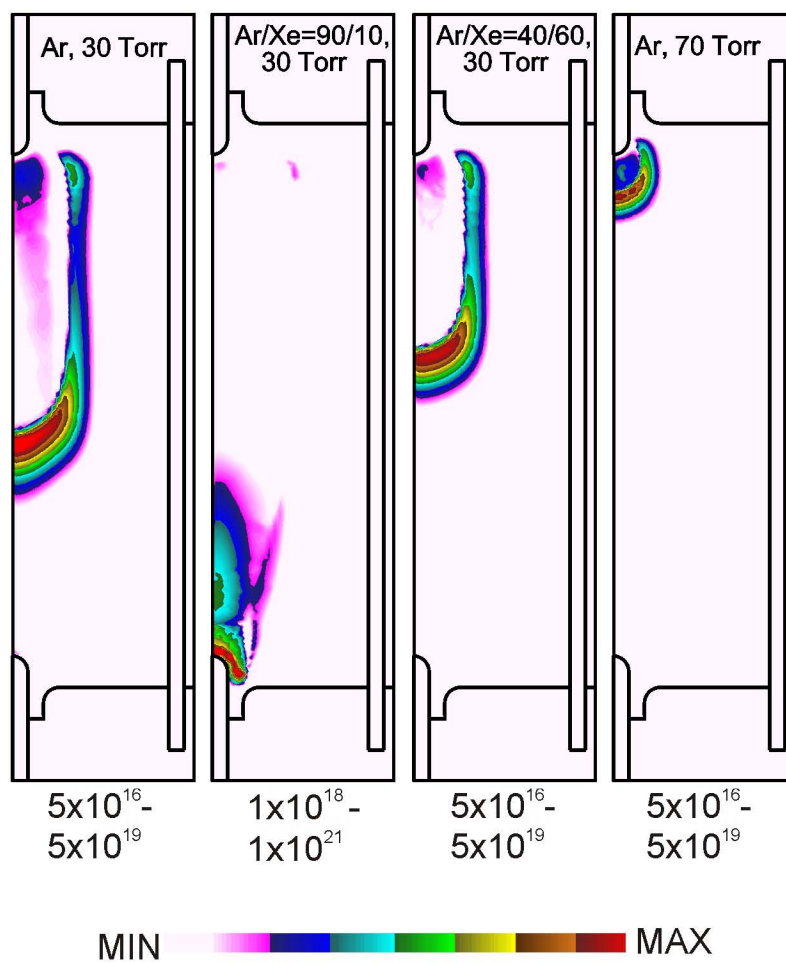


Figure 3.15 Ionization sources (log scale, $\text{cm}^{-3}\text{s}^{-1}$) at 275 ns for different compositions and pressures.

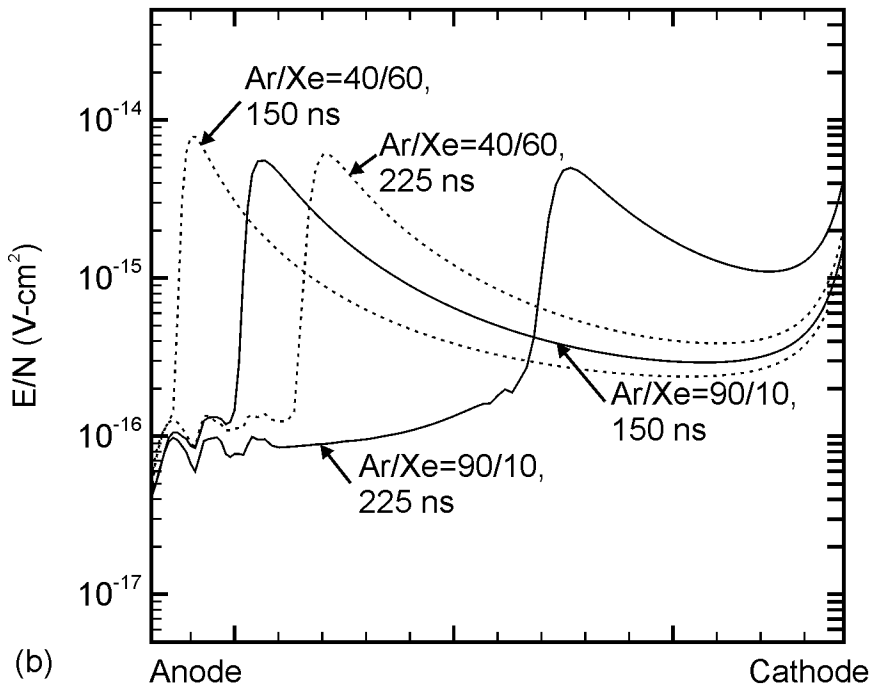
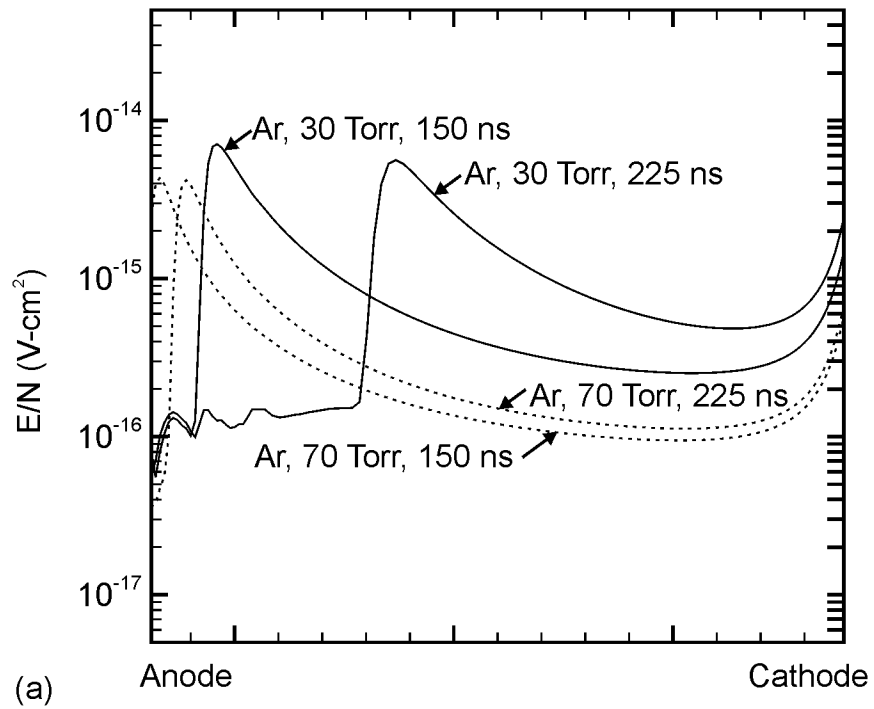
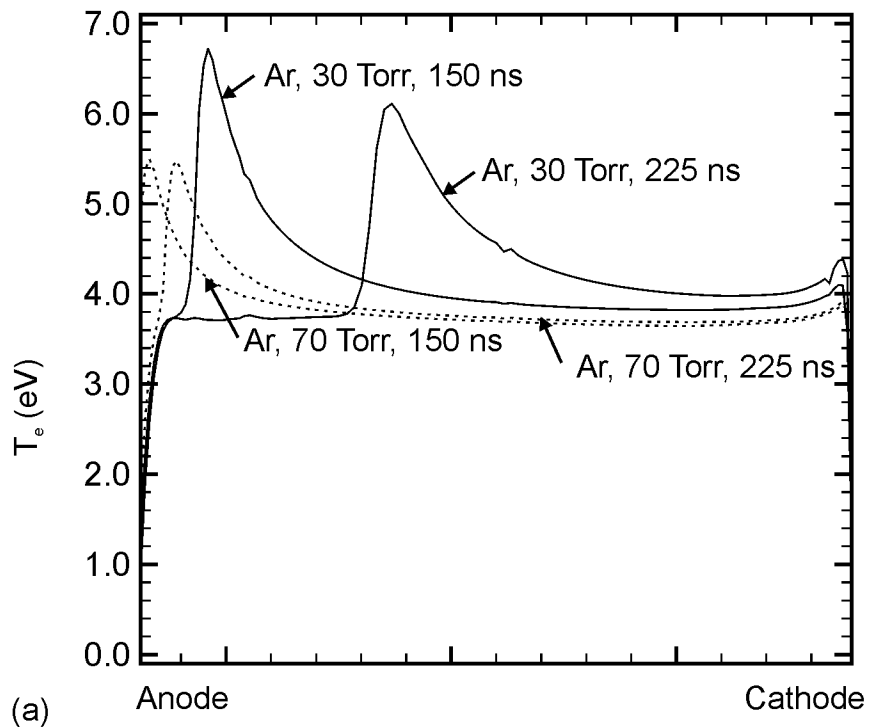
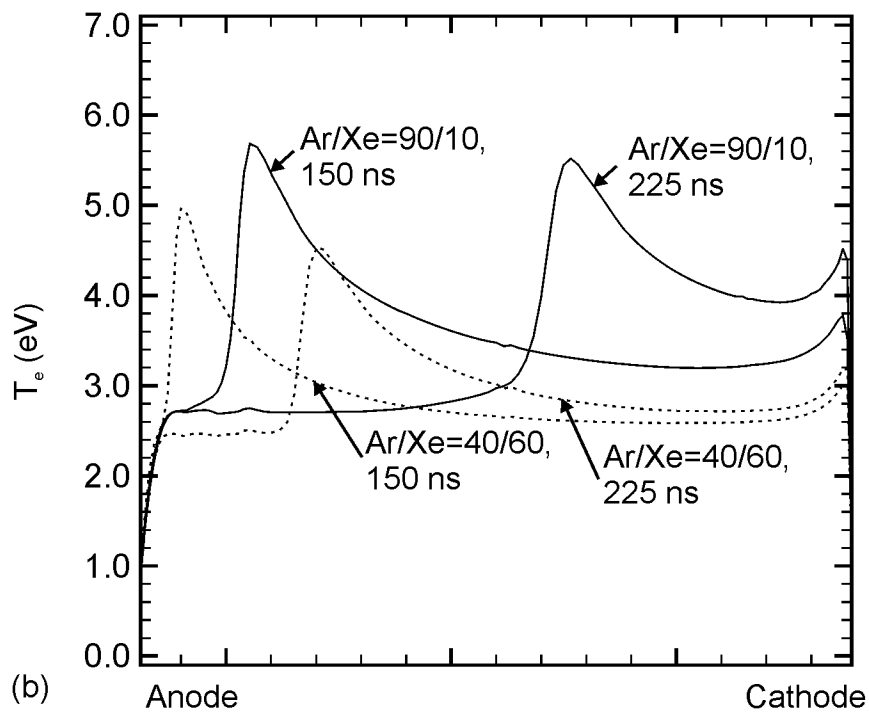


Figure 3.16 The magnitude of E/N is shown at locations along the axis of the arc tube at different instants during the breakdown event for $V_0=2000$ V and (a) Ar at 30 Torr and 70 Torr, (b) Ar/Xe=90/10 and Ar/Xe=40/60 at 30 Torr.



(a)



(b)

Figure 3.17 The electron temperature (T_e) is shown at locations along the axis of the arc tube at different instants during the breakdown event for $V_0=2000$ V and (a) Ar at 30 Torr and 70 Torr, (b) Ar/Xe=90/10 and Ar/Xe=40/60 at 30 Torr.

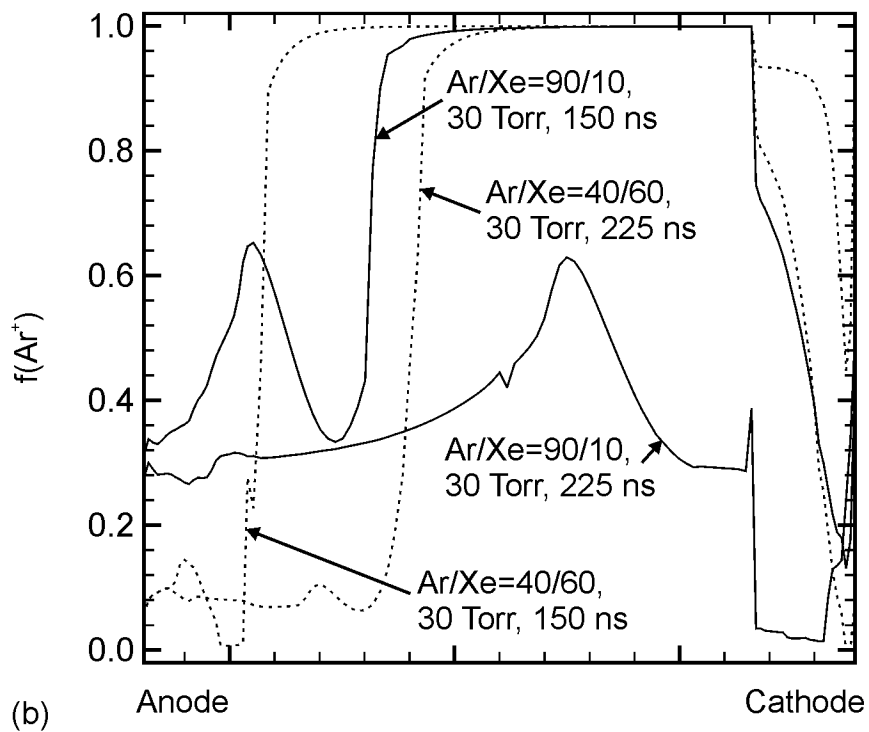
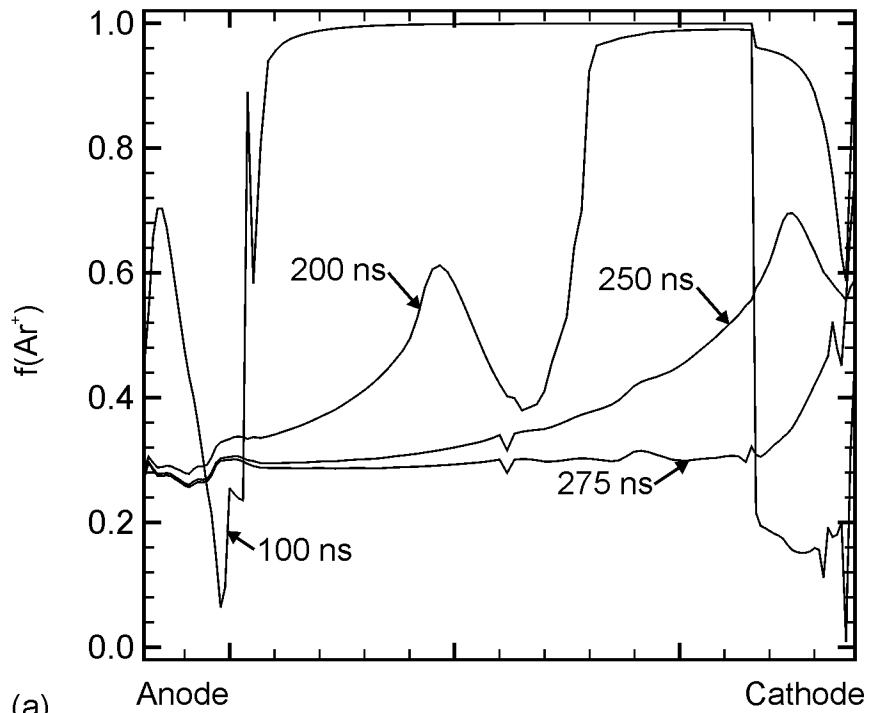


Figure 3.18 The fraction of Ar^+ ions is shown at locations along the axis of the arc tube at different instants during the breakdown event for 30 Torr, 2000 V (a) Ar only, (b) Ar/Xe=90/10 and Ar/Xe=40/60 at 150 ns and 225 ns.

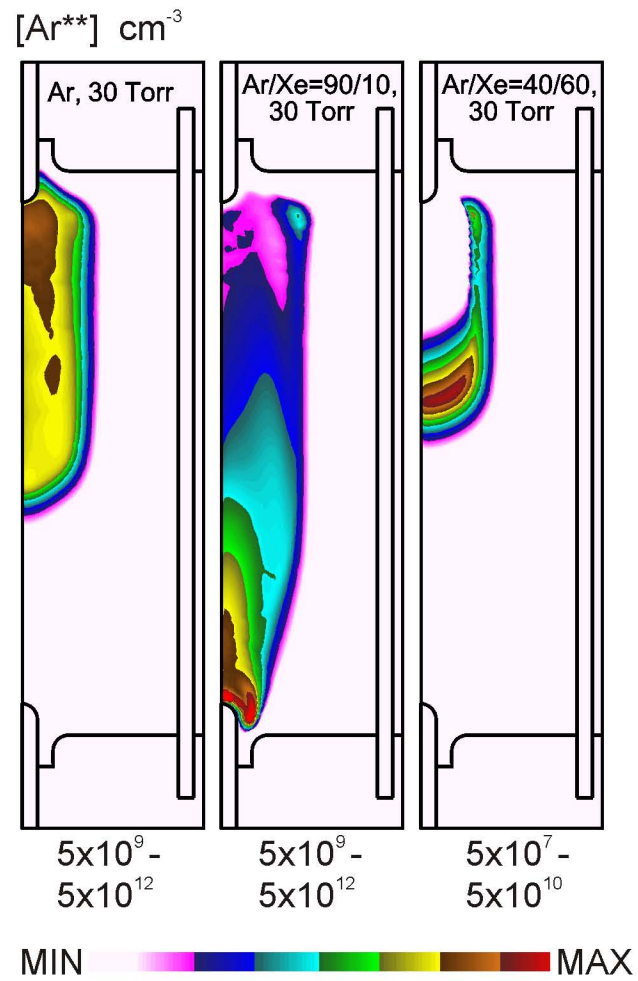


Figure 3.19 Effect of composition on Ar** density at 275 ns for $V_0=2000$ V.

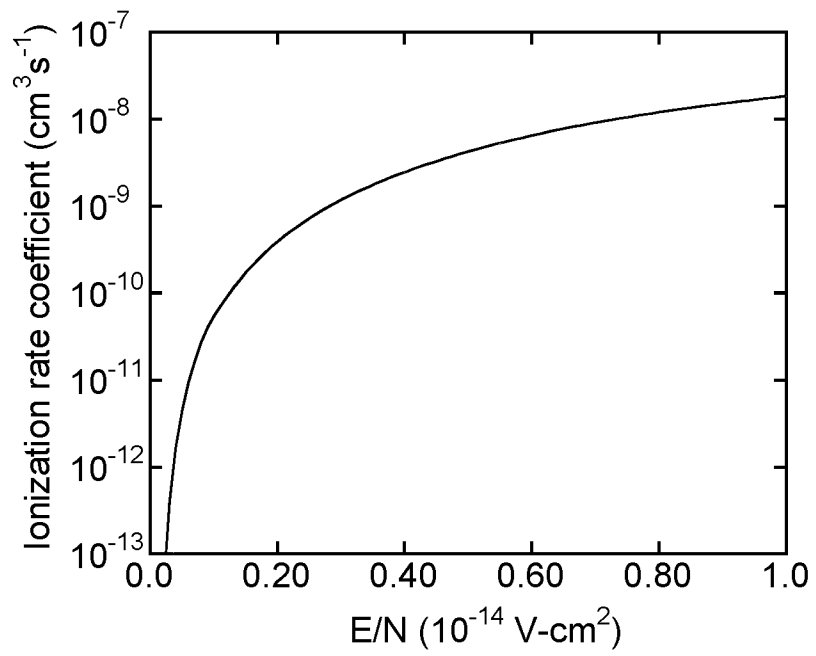


Figure 3.20 Variation of the ionization rate coefficient for Ar with applied E/N.

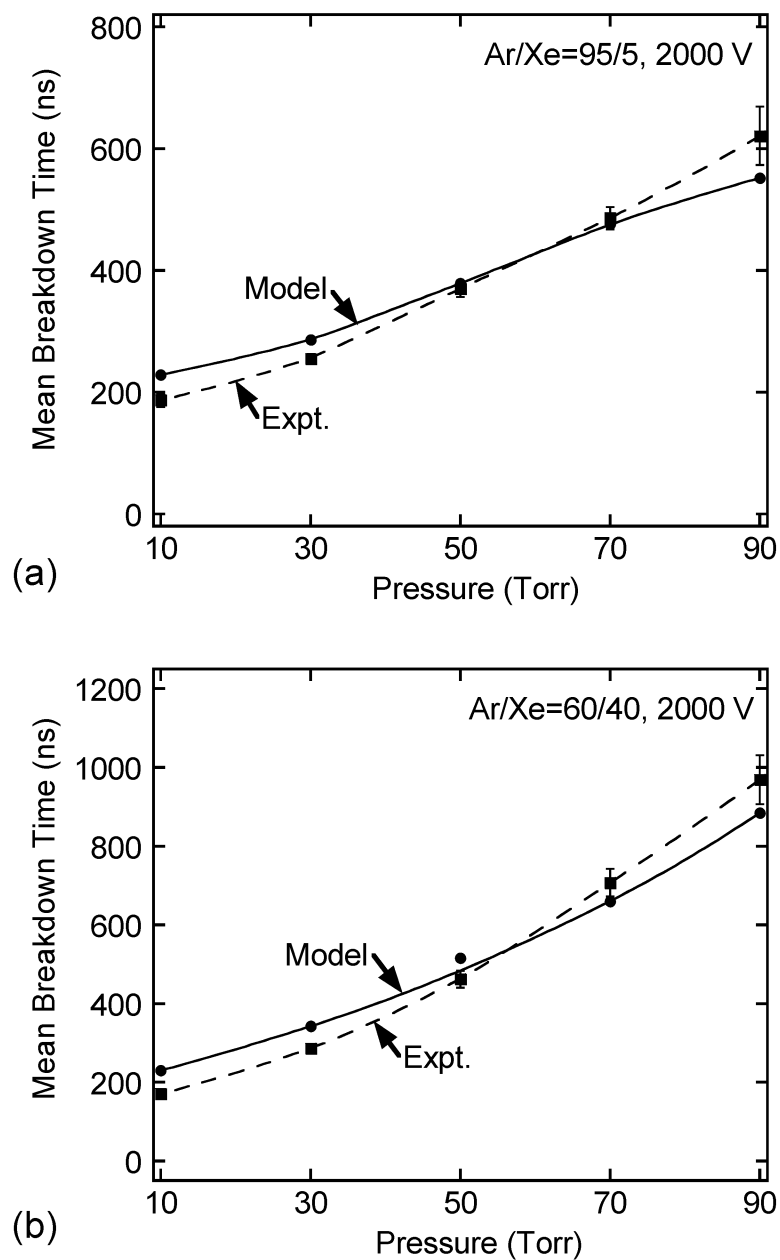


Figure 3.21 Effect of pressure on the breakdown times in Ar/Xe mixtures using the two-dimensional model for (a) Ar/Xe = 95/5, 2000 V, (b) Ar/Xe = 60/40, 2000 V and (c) Ar/Xe = 90/10, 1800 V.

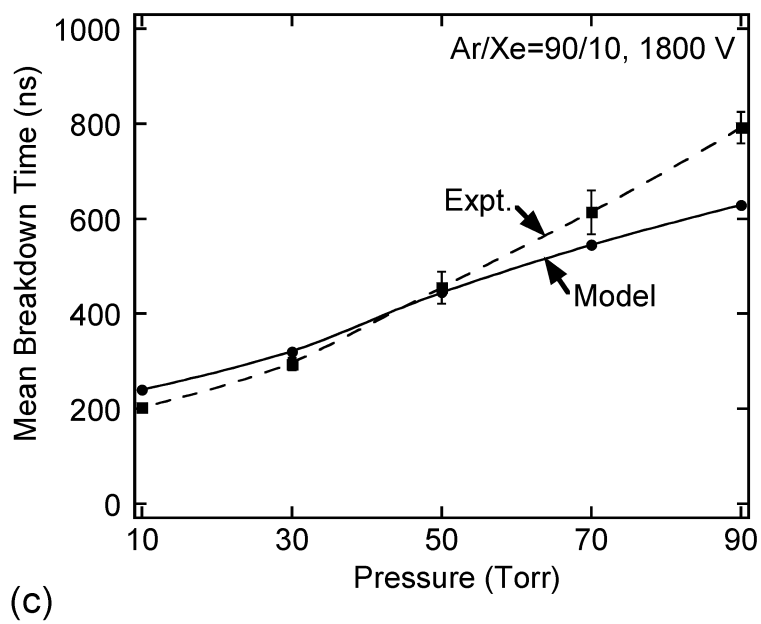


Figure 3.21, cont.

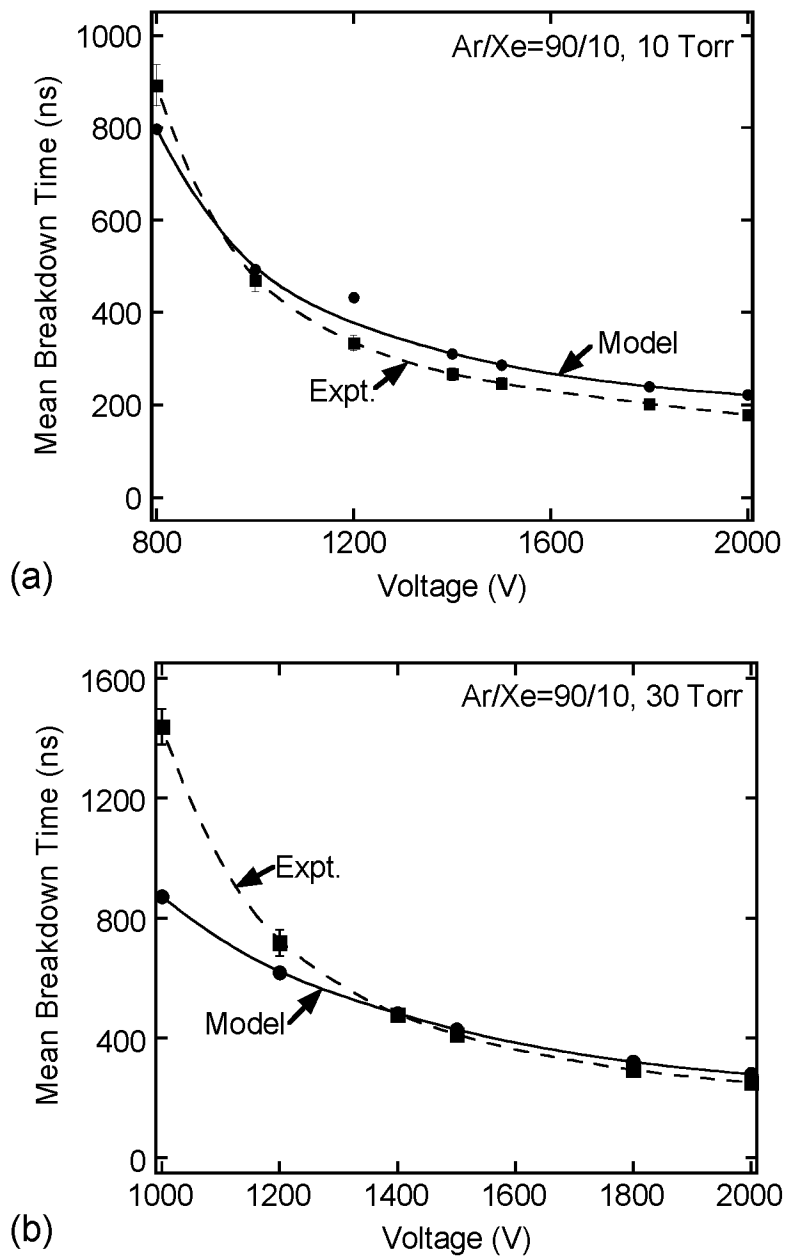
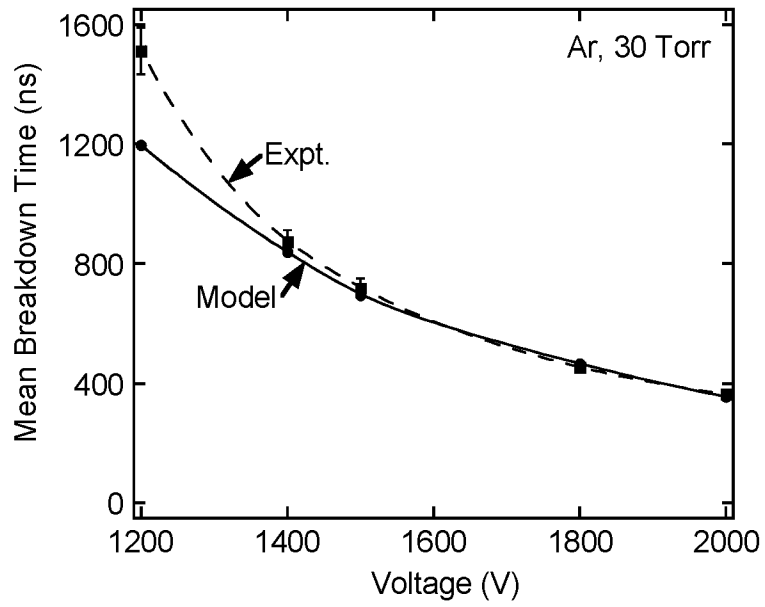


Figure 3.22 Effect of voltage on the breakdown times in Ar/Xe mixtures using the two-dimensional model for
 (a) Ar/Xe = 90/10, 10 Torr.
 (b) Ar/Xe = 90/10, 30 Torr.
 (c) Ar, 30 Torr.



(c) Figure 3.22, cont.

3.7 References

- ¹ R. S. Moss, M.S. thesis, University of Illinois at Urbana-Champaign, 2002.

4. HYDRODYNAMIC EFFECTS DURING STARTUP PHASE

4.1 Introduction

At the end of the breakdown phase a cathode fall region, characteristic of the glow phase, forms and imparts energy to ions from the negative glow. These ions bombard the cathode with significant energy resulting in sputtering of electrode material. The glow phase is thus not an efficient mode of operation compared to the thermionic arc, which is characterized by a small cathode fall and electron emission from the heated cathode sustaining the discharge. Studies have been undertaken to model steady state conditions after this phase. Charrada et al.¹, developed a two-dimensional fluid model to describe deviations from local thermal equilibrium in a high-pressure mercury arc.

The temporal range of plasma dynamics simulations can be extended beyond the breakdown phase into the glow phase by adding an ambipolar electrostatics module, which is described in Section 4.2. In the glow phase gas heating becomes significant and leads to the development of thermal gradients. Hydrodynamic motion arising as a result of these temperature gradients is addressed by a fluid dynamics module, which was integrated into the LAMPSIM platform to better capture transients in the immediate post-breakdown phase. An outline of the fluid module is presented in Section 4.3. A description of the interfacing of the fluid module with LAMPSIM is described in Section 4.4. The inclusion of hydrodynamics influences plasma dynamics and the resulting effects on plasma properties are presented in Section 4.5. A brief conclusion is given in Section 4.6.

4.2 The Ambipolar Module

In the glow phase, approximately equal densities of positive ions and electrons result after breakdown, so the net space charge in much of the plasma is usually negligible compared to the plasma density. However, some regions, especially the cathode fall, would still show charge separation in the glow phase. In addition to axial movement across the interelectrode gap, electrons and ions drift radially towards the walls as well. The walls acquire a negative charge in the early breakdown phase as a result of higher electron mobility. This serves to reduce the flux of electrons by providing a retarding potential and accelerates positive ions increasing the positive ion flux. Conditions in much of the plasma are close to quasineutrality.

In modeling the breakdown phase using LAMPSIM, Poisson's equation (3.4), charged species transport equations (3.5) and surface charge balance (3.6) are solved to obtain the electric potential and charged species densities. The time step of integration in an explicit technique is constrained by several factors, most prominent being the dielectric relaxation limit (τ_{DRT}), defined as

$$\tau_{\text{DRT}} = \frac{\varepsilon}{\sigma} \quad (4.1)$$

where σ is the conductivity and ε is the permittivity of the plasma. The dielectric relaxation limit on breakdown time scales is of the order of 10^{-12} s. Employing implicit techniques in the solution of (3.4)-(3.6), time steps of integration up to nanoseconds can be achieved with a reasonable iterative solver work. At the high plasma densities after breakdown, plasma conductivity increases, reducing the maximum time step of integration possible slowing down the solution process, and reducing the temporal range that can be addressed.

In order to address this issue, the ambipolar module (AM) was developed. The AM allows for quasineutrality in the plasma and solves for ambipolar electric potential using current conservation under conditions of high plasma density. With the net charge flux to the walls being zero, surface charge is held fixed to the value at the time of starting the AM. Since it is possible for plasma nodes away from the main discharge to be far from quasineutrality, an algorithm to determine AM nodes (those plasma nodes where AM equations would be solved) was implemented. This algorithm checks if the plasma node has a high enough electron density and if the net charge density is small enough to satisfy the quasi-neutral conditions under which AM equations are valid. At all other nodes, Poisson's equation for potential continues to be solved. The equations solved at AM nodes are

$$\frac{\partial N_i}{\partial t} = -\vec{\nabla} \cdot \vec{\phi}_i + S_i \quad (4.2)$$

$$\vec{\nabla} \cdot \vec{j} + \sum_j q_j S_j = \vec{\nabla} \cdot \sum_j (q_j \vec{\phi}_j) + \sum_j q_j S_j = 0 \quad (4.3)$$

$$N_e = \sum_i N_i q_i \quad (4.4)$$

where the N_i is the species number density of ions, N_e is the electron number density, \vec{j} is the net current density, $\vec{\phi}_j$ is the flux of species j , S_j is the source term for species j , q is the elementary charge, j loops over all charged species, and i refers to ions.

This system of Equations (4.2)-(4.4) is of a form similar to the Poisson-transport system of Equations (3.4)-(3.6). After a high plasma density is achieved, the system of equations being solved is switched from the Poisson-transport to the AM module. The solution technique employed here is therefore the same as the one implemented for

equations (3.4)-(3.6). The equations are linearized about the current solution. Jacobian components of the variables determining the system state are then numerically computed. The sparse matrix solver, *dslucs*,² is used to solve for the electric potential and charged species densities as before. Variable time stepping is used, adjusting the current time step according to the work required over a specified number of previous time steps. Since this system of equations is not limited by τ_{DRT} limit, larger time steps of integrations are possible.

4.3 The Fluid Dynamics Module

During the breakdown phase, gas heating was neglected and diffusive transport was assumed to dominate in the gas, since there are no external induced flows. However, increase in the plasma density increases power deposition and leads to a significant rise in gas temperature after breakdown. Power deposition is nonuniform in the plasma, and temperature gradients develop leading to internally generated flow. In the post-breakdown phase, therefore, convection is an important mechanism of neutral transport. Convection at steady state has been studied in the case of high-pressure mercury lamps.³

In order to address internally generated convective flows, a Navier-Stokes fluid model is used. This fluid module was developed to study buoyancy induced flows and convective flows in the context of CVD reactors.^{4, 5} Briefly, the fundamental equations solved in the fluid module are given below.

$$\frac{\partial p}{\partial t} + \vec{\nabla} \cdot (\rho \vec{v}) = 0 \quad (4.5)$$

$$\frac{\partial \rho \vec{v}}{\partial t} + \vec{\nabla} \cdot (\rho \vec{v} \vec{v}) = -\vec{\nabla} p + \vec{\nabla} \cdot \left(\mu \left(\vec{\nabla} \vec{v} + (\vec{\nabla} \vec{v})^T - \frac{2}{3} (\vec{\nabla} \vec{v}) \cdot \mathbf{I} \right) \right) - \rho \vec{g} + \vec{S}_{\text{M,plasma}} \quad (4.6)$$

$$\frac{\partial}{\partial t}(\rho C_p T) + \vec{\nabla} \cdot (\rho C_p T \vec{v}) = -\vec{\nabla} \cdot (k \vec{\nabla} T) + S_{E,plasma} \quad (4.7)$$

$$\rho = \frac{P_0 M_w}{R_g T} \quad (4.8)$$

where P_0 is operating pressure, C_p is the heat capacity (constant pressure), M_w is the molecular weight of the gas, ρ is the gas density, T is the gas temperature, \vec{v} is the gas velocity, and R_g is the ideal gas constant. The additional terms in the momentum and energy equations account for source terms to the neutral fluid arising from the presence of the plasma and are given by the expressions,

$$\vec{S}_{M,plasma} = \sum_k \sum_i \sigma_{i,k} \frac{2M_i M_k}{(M_i + M_k)^2} N_i N_k M_k v_{th} (\vec{v} - \vec{v}_i) \quad (4.9)$$

$$S_{E,plasma} = \sum_i q_i \vec{\phi}_i \cdot \vec{E} + \sum_r H_r \quad (4.10)$$

where $\vec{S}_{M,plasma}$ is the momentum source term accounting for ion-neutral collisions that result in momentum transfer to neutrals arising from motion of ions in the electric field and $S_{E,plasma}$ is the source term for the energy equation accounting for ion joule heating and heats of reaction, i denotes species that are ions, k denotes neutral species, M_i denotes molecular mass of species i (ions or neutrals), v_{th} is the thermal speed, \vec{v}_i is the velocity of ion species i , H_r is the heat of reaction r , and other symbols have their usual meaning.

The continuity equation (4.5), Navier-Stokes' equations for momentum (4.6) and the energy equation (4.7) are solved to determine the gas temperature, velocity, and density throughout the domain. The ideal gas law (4.8) is used to relate density to pressure. The fluid domain is meshed using a stair step algorithm in order to track the geometry and the elements are quadrilaterals. However, the mesh is similar to

unstructured meshes in the sense that nodes are tracked using node numbers rather than the (i, j) coordinates. The solution technique consists of solving Equations (4.5)-(4.8) on this two-dimensional mesh using second order finite volume techniques. The SIMPLE method is employed for pressure correction. Thermodynamic quantities such as the gas thermal conductivity and viscosity are calculated from fundamental formulae.⁶

4.4 Interfacing the Fluid Module and LAMPSIM

The Navier-Stokes fluid code is implemented on its own mesh and therefore a wrapper to interface it to LAMPSIM was implemented. Since the fluid code has the plasma region as its only domain, a scheme to extract the plasma domain boundary to the fluid code from the input geometry information was implemented. The mesh generation program for the fluid code was integrated into the plasma code. In order to minimize computational work, interpolation routines between the fluid mesh and the unstructured LAMPSIM mesh were set up before the start of the dynamic simulation. Simple algorithms were coded to implement these measures and are described below. The integration of the fluid code into LAMPSIM is shown in Figure 4.1.

4.4.1 Automated fluid mesh generation

A stencil covering nodes that are plasma neighbors defines the boundary of the plasma region. It is possible for the lamp to have complex structures especially near the electrodes. It was necessary to develop an algorithm to order the plasma boundary nodes in a compatible format (counter-clockwise order) so that the fluid code could read the information and perform mesh generation tasks. In the descriptions below, the word

boundary refers to the plasma boundary on the LAMPSIM mesh, which is the defining outer boundary of the domain for the fluid code.

The geometry used for the example presented in this chapter is shown with the Skymesh2 meshing and automated fluid code meshing in Figure 4.2. It is possible to specify higher refinement than shown for the fluid mesh with negligible computational overhead. In 2-D, the boundary is essentially a sequence of line segments or portions of arcs. An algorithm based on boundary tracing was developed to order the nodes comprising the boundary. The algorithm starts with a boundary node, then finds the two nearest boundary nodes and uses 0 and 1 to represent directions with respect to the present boundary node. An array keeps track of whether a boundary node has been ordered. Using node coordinates, it is possible to start with the boundary node closest to the axes. In an axisymmetric case, this node would have just one nearest boundary neighbor. Then using the search direction code and tracking array, the entire boundary is ordered in a counter-clockwise direction.

Automating the fluid mesh generation requires boundary conditions in addition to ordered boundary nodes. Properties of the LAMPSIM mesh were utilized for this purpose. The mesh generation process for the fluid code was thus converted entirely into an internal task.

4.4.2 Interpolation setup

Neutral flows normally reach convergence on the order of 10s of μs to ms. In this simulation, our interest lies in the hydrodynamic effects that occur on the timescales of plasma dynamics. Calls to the fluid code are therefore made on a less frequent basis than

the integration of the plasma dynamics. The time step of integration for the fluid module is normally 50-100 times that used in the plasma dynamics. In between calls, gas temperature and velocity fields are assumed not to vary. The intention is to capture transient effects of fluid motion on the plasma dynamics in the early glow phase. Quantities interpolated between the meshes include the source terms for momentum and energy from the LAMPSIM mesh to the fluid mesh. Gas temperatures and velocities calculated in the fluid code are interpolated back to the LAMPSIM mesh from the fluid mesh on completion of one time step of integration using interface function calls.

The scheme used to interpolate from LAMPSIM to the fluid mesh is shown in Figure 4.3. Every fluid mesh cell has a local horizontal and vertical axis. These local axes divide the two-dimensional space around the cell into four quadrants denoted by I to IV. In each quadrant there may be zero, one, or more triangular nodes since the fluid mesh is usually more highly refined. To identify triangular nodes in each quadrant, search algorithms are implemented. In case no triangular nodes are found, the search is expanded until at least one triangular node is found in each quadrant. If more than one triangular node is present in a particular region, distances are computed from the fluid mesh cell location and only the closest node is considered for interpolation. Once a triangular node is identified in each quadrant, they are interpolated onto the local X and Y axes by constructing chords. Standard finite difference techniques are then used to determine the interpolated value on the mesh cell.

Interpolation from the fluid mesh to LAMPSIM starts by locating the cell centers closest to the LAMPSIM node. This is accomplished by determining the coordinates of

the node and hence the particular (i, j) interval it would fall into on the fluid mesh as depicted in Figure 4.4. To interpolate a general variable ϕ , it is expressed in the form

$$\phi(x, y) = c_1 + c_2x + c_3y + c_4xy \quad (4.11)$$

where c_1, c_2, c_3 , and c_4 are determined by solving the system of equations given by

$$\begin{pmatrix} 1 & x_1 & y_1 & x_1y_1 \\ 1 & x_2 & y_2 & x_2y_2 \\ 1 & x_3 & y_3 & x_3y_3 \\ 1 & x_4 & y_4 & x_4y_4 \end{pmatrix} \begin{pmatrix} c_1 \\ c_2 \\ c_3 \\ c_4 \end{pmatrix} = \begin{pmatrix} \phi_1 \\ \phi_2 \\ \phi_3 \\ \phi_4 \end{pmatrix} \quad (4.12)$$

and $\phi_1, \phi_2, \phi_3, \phi_4$ are known at the four mesh cells.

These interpolation constants are calculated only once and stored.

4.5 Interaction of Plasma Dynamics and Hydrodynamics

The integrated fluid module-plasma dynamics model was used to investigate the variation of gas temperature and plasma properties during breakdown and early glow phase. In the base case presented here, the lamp geometry is similar to that shown in Figure 3.1 with some minor modifications. In this case, the upper electrode is grounded while the lower electrode is powered. The interelectrode gap is now maintained at 0.8 cm. The base case conditions correspond to pure Ar gas-fill at 70 Torr. The reaction mechanism is found in Appendix A. The waveform of the applied voltage is shown in Figure 4.5.

4.5.1 Dynamics of gas temperature

The initial gas temperature is 300 K. On application of the voltage pulse, the electron avalanche begins near the powered electrode. The electron density and gas

temperature are shown at different times up to breakdown in Figure 4.6. The avalanche is anode-directed at 1 μs . The electron density at the leading edge of the avalanche front is 10^9 cm^{-3} , while the peak electron density (10^{11} cm^{-3}) occurs near the cathode. The gas temperature starts to marginally rise in these ionized regions because of energy deposition. At 1 μs , the rise in gas temperature is low ($\approx 0.75 \text{ K}$). By 2 μs , the electron avalanche has reached the anode and a reverse cathode-directed avalanche begins. At this time, the gas temperature in much of the plasma has started to rise above the ambient. At 4 μs , the electron avalanche reaches the cathode and large potential drop develops near it, signifying the completion of breakdown. The gas temperature is higher in regions near the cathode as a result of large electric fields and consequently larger ion joule heating than in the rest of the plasma. The peak gas temperature is about 320 K near the cathode, but the rise in gas temperature in the bulk remains marginal (0.01 – 1.5 K).

The simulation is continued into the glow phase. The electron density and gas temperature up to 10 μs are shown in the postbreakdown phase in Figure 4.7. At 6 μs , plasma density along the axis is about 10^{12} cm^{-3} . The sustained voltage at the powered electrode helps ionization of the bulk gas and increases power deposition along the axis. The gas temperature starts to rise near the electrode as well as along the axis of the arc tube. At 8 μs , gas temperature along the axis has risen by 40-60 K. Regions near the cathode are considerably more heated and the peak T_g is 585 K. Higher plasma density along the axis of the arc tube leads to a larger rise in T_g than in regions near the walls due to increased power deposition. By 10 μs , there is a considerable increase in electron density in the radial direction. The gas temperature peaks at 460 K along the axis. Significantly higher contribution due to ion joule heating is sustained in the regions as a

result of high electric fields near the cathode and leads to a much larger gas temperature than in the bulk. Peak gas temperature close to the cathode is 935 K.

4.5.2 Effect on plasma properties

Transient convection fields arising out of thermal gradients lead to perturbations in neutral density. The neutral density computed at the end of 10 μs is presented in Figure 4.8 for two cases: (a) not including hydrodynamic effects, and (b) including effects of hydrodynamics. In the first case, isothermal conditions are assumed to prevail and fluid motion is dominated by diffusion. Hence, gas density continues to remain more or less constant and uniform throughout the quartz tube. When the fluid module is used to capture hydrodynamic effects, changes in gas density are apparent. Higher T_g along the axis leads to a depletion of neutral density away from the center of the arc tube. Consequently, neutral density in regions closer to the walls increases. The depletion in density is highest in regions close to the cathode where the gas temperature peaks.

Plasma properties are closely associated with variations in the neutral density. Small changes in density lead to perturbations in E/N that can have dramatic effects on rate coefficients and hence plasma dynamics. The electron temperature at 4 μs and 10 μs is shown in Figure 4.9 for the two cases as before. At 4 μs , the electron temperatures throughout the arc tube are similar. By 10 μs , the electron temperatures start to decrease in the aftermath of breakdown. When isothermal conditions are assumed, electron temperatures in regions near the anode are in the range of 2-2.6 eV. When hydrodynamic effects are taken into account, the depletion in density leads to a rise in the local E/N in regions along the axis. The increase in E/N leads to a rise in electron temperature near the

anode to about 3-3.2 eV. Peak electron temperature near the cathode rises from 6.3 eV to 10 eV when hydrodynamic effects are included.

The ionization sources are shown in Figure 4.10 for the two cases at 4 μs and 10 μs . Again, the ionization sources at the end of the breakdown phase are not very different with or without hydrodynamic effects. The rise in electron temperature along the axis of the arc tube in turn affects ionization source terms when including hydrodynamic effects. The effect on sources is evident at 10 μs . Lower electron temperatures in the isothermal case lead to depletion of ionization sources close to the cathode and recombination starts to dominate. Higher electron temperatures as a result of hydrodynamic effects help sustain electron impact sources. The average magnitude of ionization sources is about $10^{18}\text{cm}^{-3}\text{s}^{-1}$ in the center along the axis of the arc tube. Peak ionization sources near the cathode increase to $10^{20}\text{cm}^{-3}\text{s}^{-1}$ from $5 \times 10^{19}\text{cm}^{-3}\text{s}^{-1}$ with the isothermal assumption.

4.6 Conclusions

Hydrodynamics were integrated into LAMPSIM to capture transient effects of gas heating in the early glow phase. In the breakdown phase, energy deposition is low and gas heating is negligible. As the plasma density starts to increase in the post breakdown period, energy deposition increases. Nonuniform plasma conditions lead to nonuniform energy deposition and development of thermal gradients, first near the powered electrode and later in the bulk plasma. Internally generated convective flow transients deplete neutral density at the center of the arc tube. Perturbations in E/N arising out of small changes in density lead to rapid and significant changes in plasma properties.

4.7 Figures

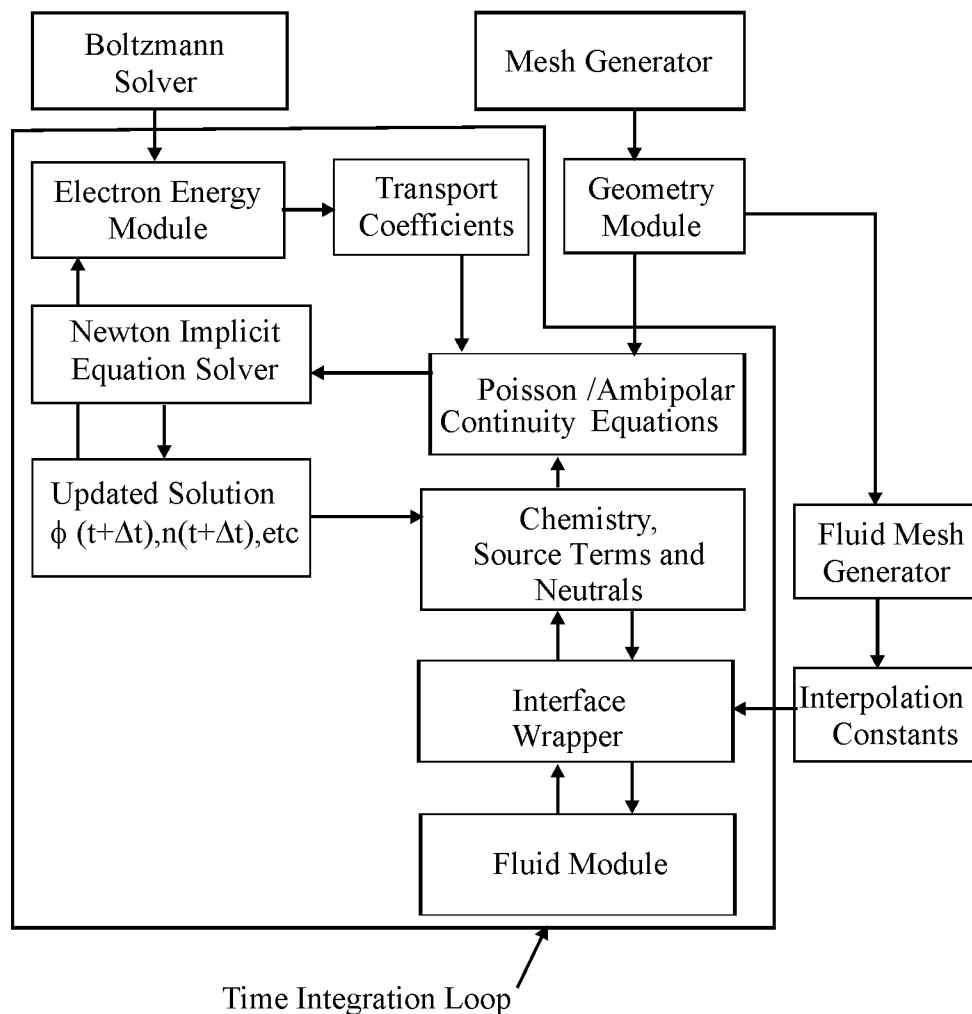
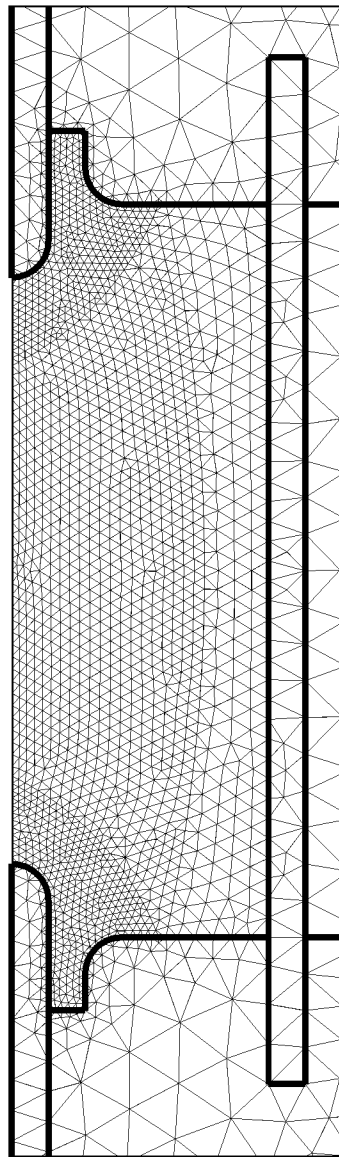
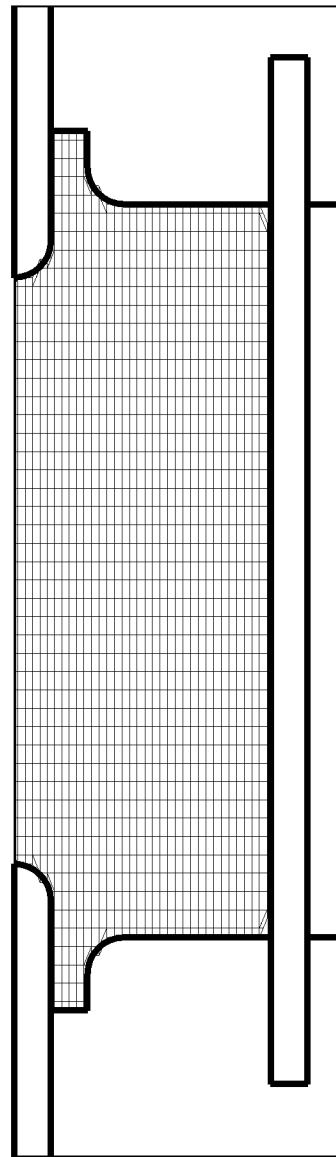


Figure 4.1 Interfacing the Navier-Stokes fluid module to LAMPSIM: Source terms are used as input to the fluid module and gas velocity and temperature is returned for use in LAMPSIM in updating reaction sources.



LAMPSIM mesh



Fluid Module mesh

Figure 4.2 The LAMPSIM mesh (left) and the fluid mesh (right) for the geometry considered in the base case. The fluid mesh shown here is coarser than that used in the simulation.

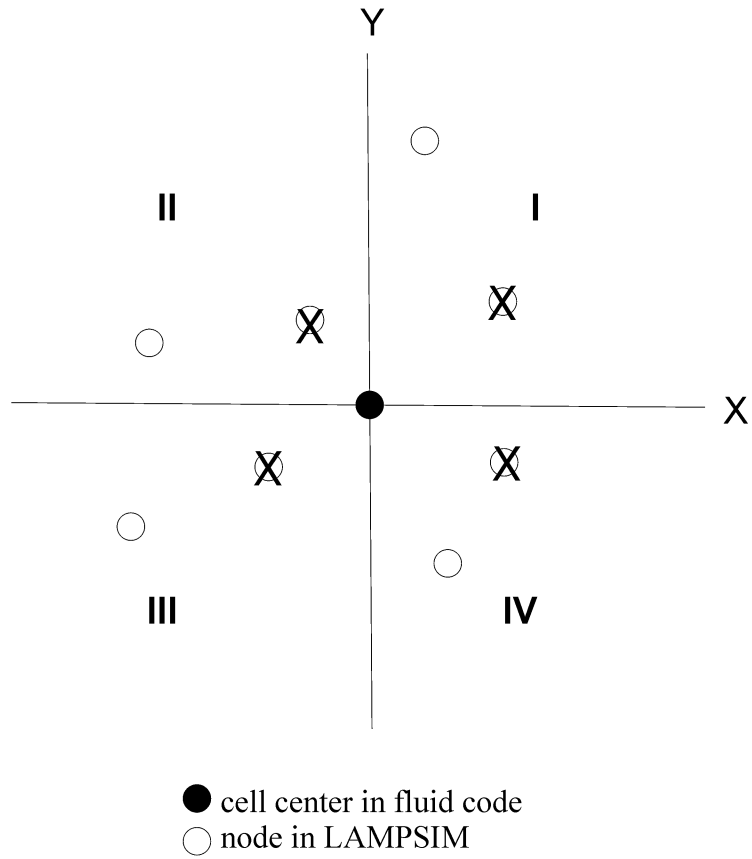


Figure 4.3 Interpolation from the LAMPSIM mesh to the fluid mesh: Each fluid mesh cell may have several triangular nodes in each of the four quadrants defined by the local X and Y axes. The nearest node in each quadrant (marked by the X sign over it) is located for interpolation.

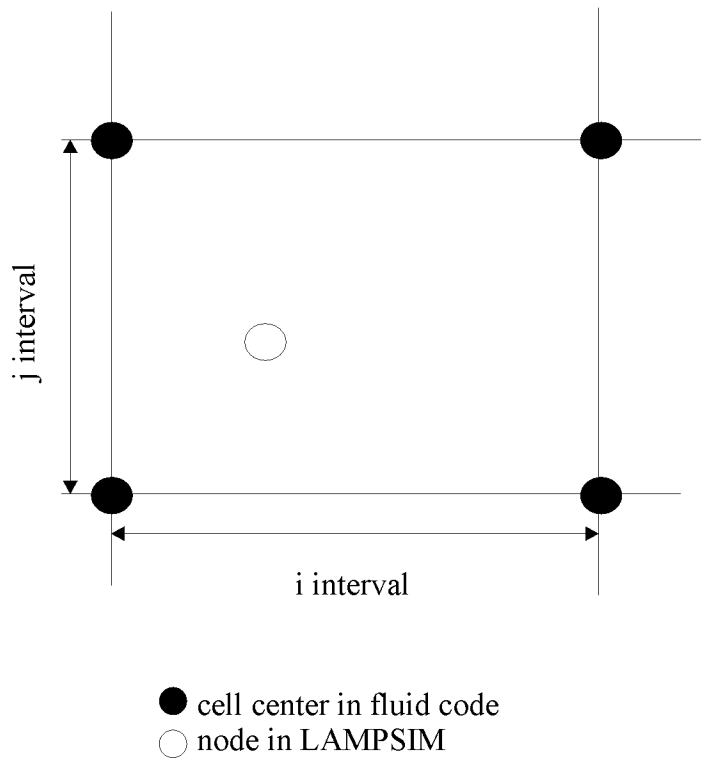


Figure 4.4 Interpolation from Fluid Module mesh to LAMPSIM mesh: Each LAMPSIM node location is surrounded by four fluid mesh cells. These cells are located and mapped onto each triangular node in the plasma.

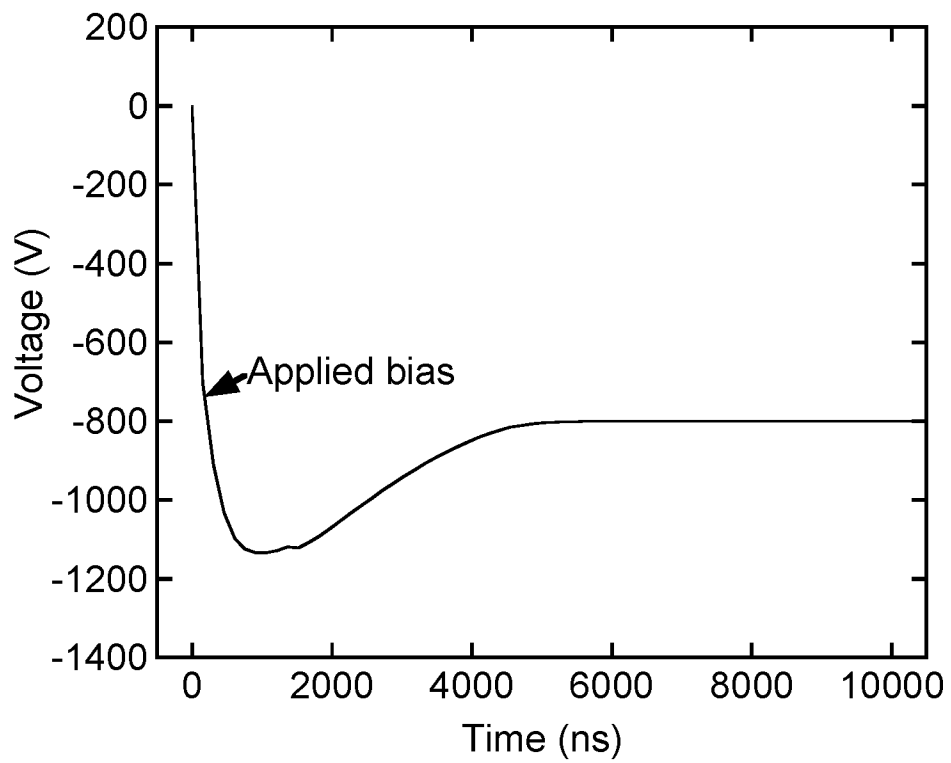


Figure 4.5 The voltage waveform used for the base case (Ar 70 Torr).

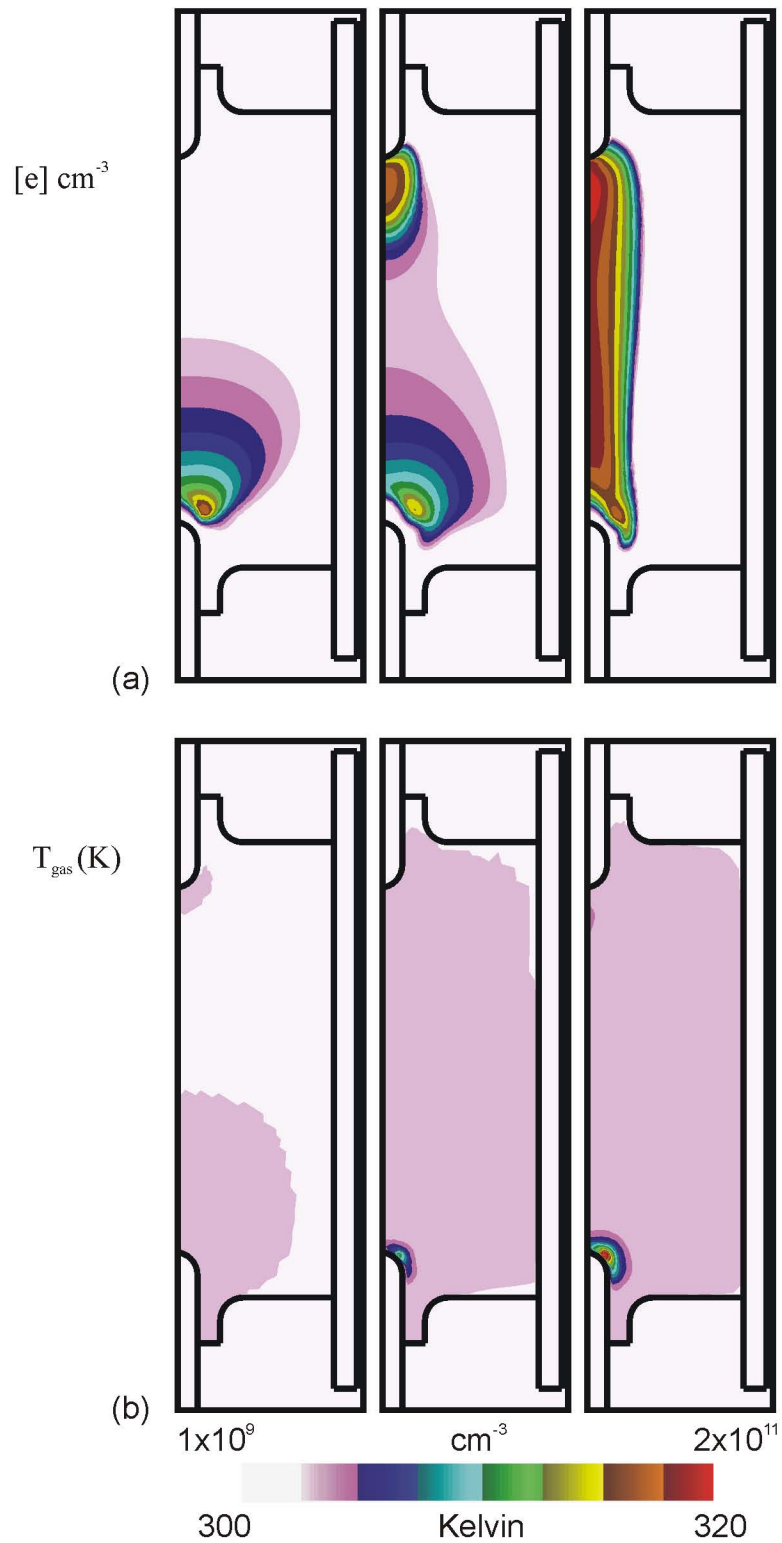


Figure 4.6 (a) Electron density (log scale) and (b) gas temperature (linear scale) for the base case conditions (Ar 70 Torr, -800 V). The frames (from left to right) denote conditions at $1 \mu\text{s}$, $2 \mu\text{s}$, and $4 \mu\text{s}$, respectively.

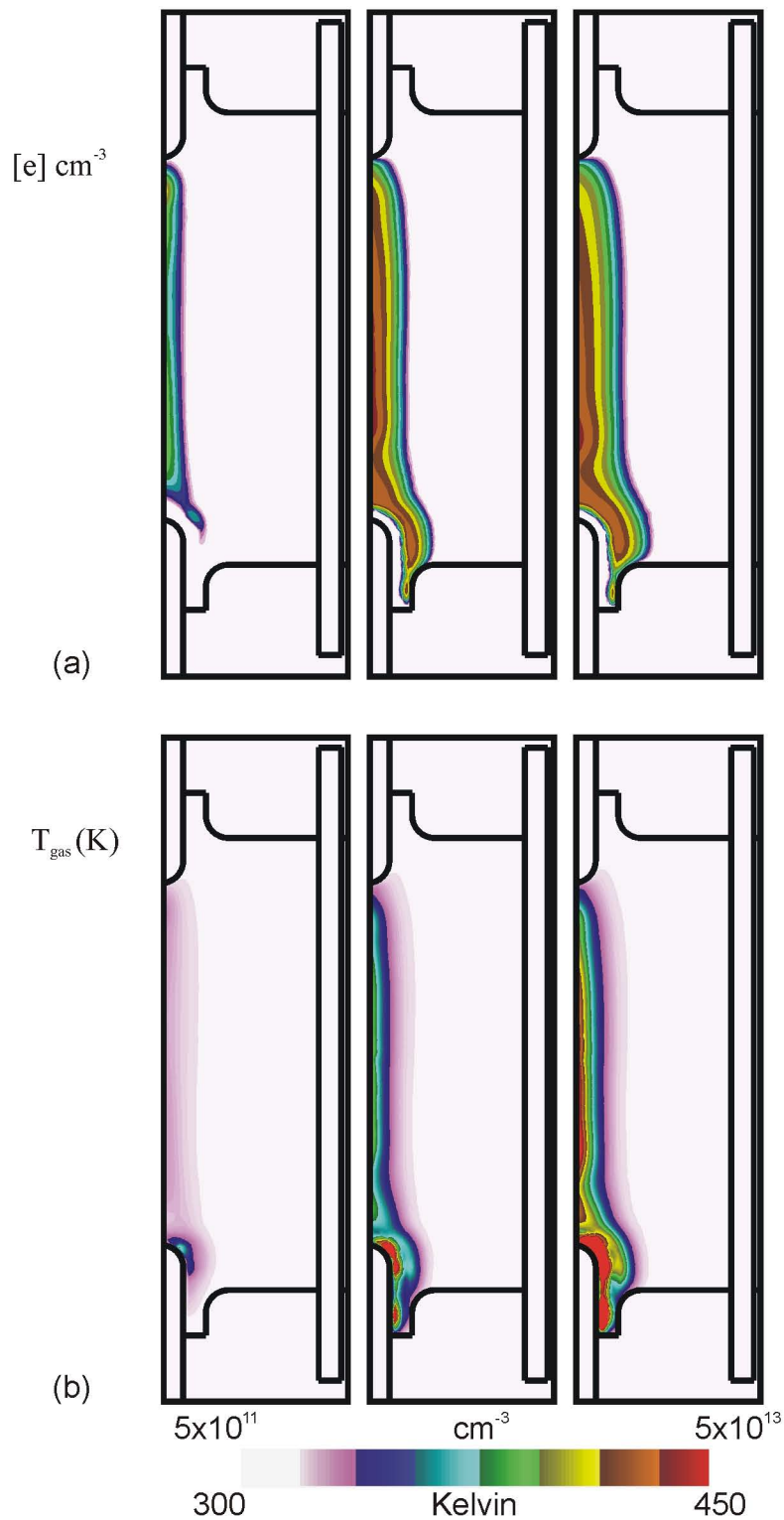


Figure 4.7 (a) Electron density (log scale) and (b) gas temperature (linear scale) for the base case conditions (Ar 70 Torr, -800 V). The frames (from left to right) denote conditions at 6 μs , 8 μs , and 10 μs , respectively.

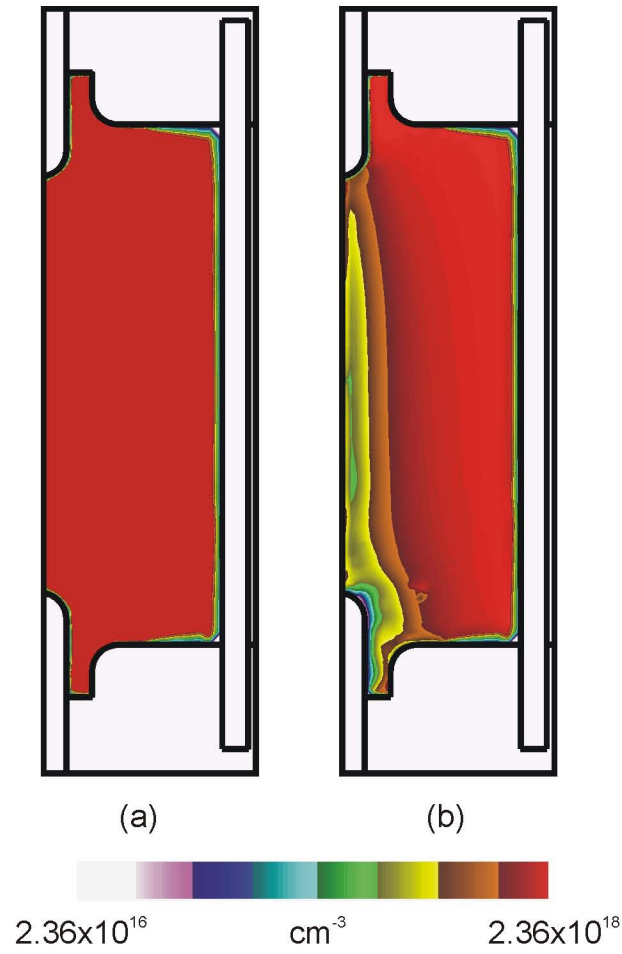


Figure 4.8 Neutral density for base case conditions (Ar 70 Torr, -800 V) at $10 \mu\text{s}$ when (a) hydrodynamics is not included and (b) including hydrodynamics.

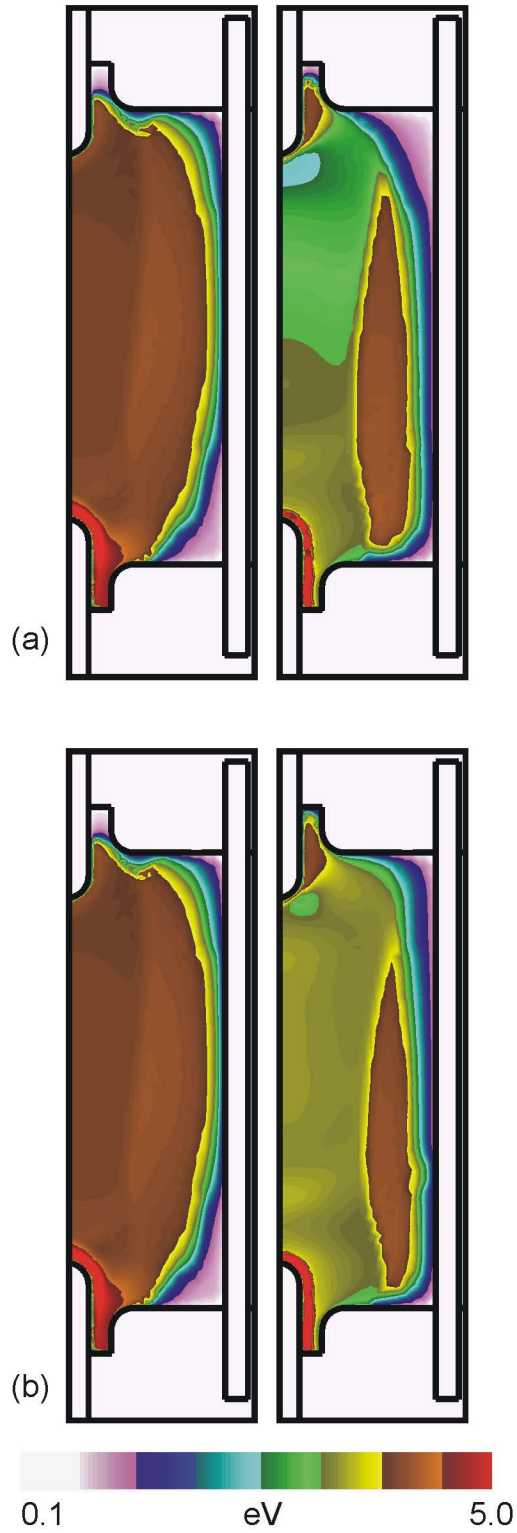


Figure 4.9 Electron temperature for base case conditions (Ar 70 Torr, -800 V) at (left to right frame) $4 \mu\text{s}$ and $10 \mu\text{s}$ when (a) hydrodynamics is not included and (b) including hydrodynamics.

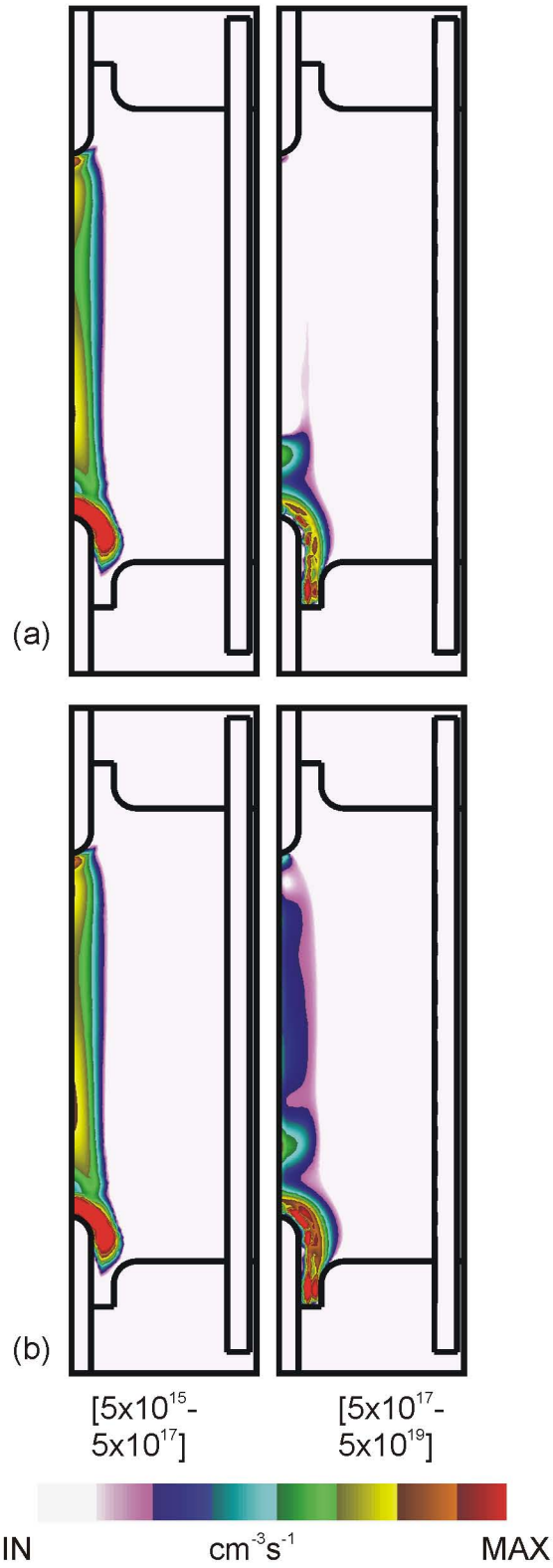


Figure 4.10 Ionization sources (log scale) for base case conditions (Ar 70 Torr, -800 V) at (left to right frame) 4 μs and 10 μs when (a) hydrodynamics is not included and (b) including hydrodynamics.

4.8 References

- ¹ K. Charrada, G. Zissis, and M. Aubes, *J. Phys. D: Appl. Phys.* **29**, 2432 (1996).
- ² SLAP Sparse Matrix Library, <http://www.netlib.org>
- ³ P. Y. Chang, W. Shyy, and K. T. Dakin, *Int. J. Heat Mass Transfer* **33**, 483 (1990).
- ⁴ G. Luo, Ph.D. Dissertation, University of Illinois at Urbana-Champaign, 2003.
- ⁵ S. P. Vanka, G. Luo, and N. G. Glumac, *J. Heat Transfer* (accepted).
- ⁶ J. O. Hirschfelder, C. F. Curtiss, and R. B. Bird, *Molecular Theory of Solids and Liquids* (John Wiley and Sons, University of Wisconsin, 1965).

5. CONCLUSIONS

In the work reported on in this thesis basic physical processes occurring during the breakdown processes in high intensity discharge lamps were investigated. Breakdown was studied in Ar/Xe mixtures that have many of the same qualitative characteristics of Ar/Hg mixtures found in metal halide lamps. Zero-dimensional and two-dimensional models were used and results obtained from these models facilitated comparison to experiments. Parameterizations were performed to obtain trends in breakdown times with composition, pressure, and applied voltage. While results from the zero-dimensional model were consistent with experiments, there were substantial quantitative differences. The two-dimensional model addressed these discrepancies by describing the spatial evolution of breakdown dynamics. The results predicted from the two-dimensional model closely tracked experimentally observed values over a range of compositions, pressures, and applied voltages.

After breakdown occurs, the plasma density starts to increase in the discharge tube. At high plasma densities, the dielectric relaxation time becomes a constraining factor in the time-stepping process. In order to circumvent this limitation, an ambipolar module was added to the two-dimensional platform. This addresses similar equations as the breakdown model with the exception of assuming quasi-neutrality in the plasma and hence solving for electric potential using current conservation. One of the difficulties faced was determining the time for switching to the ambipolar module. It is physically unrealistic to use the ambipolar module when the plasma density is low. On occasions,

numerical difficulties were encountered if the time for switching to the ambipolar module was delayed far beyond the breakdown time.

During the breakdown process, the energy deposition being small, there is no significant rise in gas temperature. The assumption of an isothermal gas mixture is valid for the breakdown phase. As the plasma density increases after breakdown, however, the energy deposition starts to increase. In order to capture the effects of the increased energy deposition in the early glow phase of the startup, a two-dimensional incompressible Navier-Stokes' fluid module was interfaced with the two-dimensional plasma dynamics model. This required implementing an automated mesh generation since the fluid module used a boundary fitted structured mesh. These hydrodynamics effects were studied in a metal halide lamp geometry with Ar gas fill. The resulting rise in gas temperature is spatially inhomogeneous and density gradients develop. Regions of the plasma with a higher gas temperature have lower gas density and hence E/N is higher than it would have been with an isothermal gas. Rates of reactions depend exponentially on E/N , and these small perturbations arising out of density gradients result in significantly perturbed plasma properties.

APPENDIX A: KINETICS OF Ar/Xe MIXTURES

A.1 List of Species

e	Xe	ArXe*
Ar*(4s)	Xe*(6s)	ArXe ⁺
Ar**(4p)	Xe**(6p)	
Ar ⁺	Xe*** (6s')	
Ar ₂ *	Xe ⁺	
Ar ₂ ⁺	Xe ₂ *	
	Xe ₂ ⁺	

A.2 Ar/Xe Reaction Mechanism

<u>Reaction</u>	<u>Rate coefficient^a</u>	<u>Ref.</u>
$e + \text{Ar} \rightarrow \text{Ar} + e$	b	1
$e + \text{Ar} \rightarrow \text{Ar}^* + e$	b	1
$e + \text{Ar} \rightarrow \text{Ar}^{**} + e$	b	2
$e + \text{Ar} \rightarrow \text{Ar}^+ + e + e$	b	3
$e + \text{Ar}^* \rightarrow \text{Ar}^+ + e + e$	b	4
$e + \text{Ar}^{**} \rightarrow \text{Ar}^+ + e + e$	b	5
$e + \text{Ar}_2^* \rightarrow \text{Ar}_2^+ + e + e$	$9.0 \times 10^{-8} T_e^{0.7} e^{-3.66/T_e}$	6
$e + \text{Ar}^* \rightarrow \text{Ar}^{**} + e$	b	7
$e + \text{Ar}^* \rightarrow \text{Ar} + e$	b,c	2
$e + \text{Ar}^{**} \rightarrow \text{Ar} + e$	b	2
$e + \text{Ar}^{**} \rightarrow \text{Ar}^* + e$	b	7

$e + \text{Ar}_2^+ \rightarrow \text{Ar}^{**} + \text{Ar}$	$5.38 \times 10^{-8} T_e^{-0.66}$	6
$e + \text{Ar}_2^* \rightarrow \text{Ar} + \text{Ar} + e$	1.0×10^{-7}	6
$e + \text{Ar}^+ \rightarrow \text{Ar}^{**}$	$4.0 \times 10^{-13} T_e^{-0.5}$	8
$e + e + \text{Ar}^+ \rightarrow \text{Ar}^{**} + e$	$5.0 \times 10^{-27} T_e^{-4.5} \text{ cm}^6 \text{ s}^{-1}$	8
$e + \text{Xe} \rightarrow \text{Xe} + e$	b	1
$e + \text{Xe} \rightarrow \text{Xe}^* + e$	b	9
$e + \text{Xe} \rightarrow \text{Xe}^{**} + e$	b	10
$e + \text{Xe}^* \rightarrow \text{Xe}^{**} + e$	b	11
$e + \text{Xe} \rightarrow \text{Xe}^+ + e + e$	b	3
$e + \text{Xe}^* \rightarrow \text{Xe}^+ + e + e$	b	11
$e + \text{Xe}^{**} \rightarrow \text{Xe}^+ + e + e$	b	11
$e + \text{Xe}_2^* \rightarrow \text{Xe}_2^+ + e + e$	$9.75 \times 10^{-8} T_e^{0.71} e^{-3.40/T_e}$	12
$e + \text{Xe}^* \rightarrow \text{Xe} + e$	b	9
$e + \text{Xe}^{**} \rightarrow \text{Xe}^* + e$	b	11
$e + \text{Xe}^{**} \rightarrow \text{Xe} + e$	b	11
$e + \text{Xe}_2^+ \rightarrow \text{Xe}^* + \text{Xe}$	$0.37 \times 10^{-7} T_e^{-0.5}$	8,d
$e + \text{Xe}_2^+ \rightarrow \text{Xe}^{**} + \text{Xe}$	$0.37 \times 10^{-7} T_e^{-0.5}$	8,d
$e + \text{Xe} \rightarrow \text{Xe}^{***} + e$	b	13
$e + \text{Xe}^{***} \rightarrow \text{Xe}^+ + e + e$	$1.56 \times 10^{-7} T_e^{0.71} e^{-2.63/T_e}$	12
$e + \text{Xe}^{***} \rightarrow \text{Xe}^{**} + e$	$5.50 \times 10^{-7} T_e^{0.79} e^{-2.0/T_e}$	d
$e + \text{Xe}^{***} \rightarrow \text{Xe} + e$	b	13
$e + \text{Xe}_2^+ \rightarrow \text{Xe}^{***} + \text{Xe}$	$3.33 \times 10^{-7} T_e^{-0.5}$	8,d

$e + \text{ArXe}^+ \rightarrow \text{Xe}^{**} + \text{Ar}$	$1.0 \times 10^{-7} T_e^{0.5}$	6
$e + \text{ArXe}^* \rightarrow \text{Xe} + \text{Ar} + e$	1.0×10^{-10}	12
$\text{Ar}^+ + \text{Ar} \rightarrow \text{Ar} + \text{Ar}^+$	4.60×10^{-10}	14,e
$\text{Ar}^* + \text{Ar} + \text{Ar} \rightarrow \text{Ar}_2^* + \text{Ar}$	$1.14 \times 10^{-32} \text{ cm}^6 \text{ s}^{-1}$	6
$\text{Ar}^{**} + \text{Ar} + \text{Ar} \rightarrow \text{Ar}_2^* + \text{Ar}$	$1.14 \times 10^{-32} \text{ cm}^6 \text{ s}^{-1}$	6
$\text{Ar}^+ + \text{Ar} + \text{Ar} \rightarrow \text{Ar}_2^+ + \text{Ar}$	$2.50 \times 10^{-31} \text{ cm}^6 \text{ s}^{-1}$	6
$\text{Ar}_2^* \rightarrow \text{Ar} + \text{Ar}$	$6.0 \times 10^7 \text{ s}^{-1}$	6
$\text{Ar}^{**} \rightarrow \text{Ar}$	$2.0 \times 10^6 \text{ s}^{-1}$	d
$\text{Ar}^* \rightarrow \text{Ar}$	$1.0 \times 10^1 \text{ s}^{-1}$	15,g
$\text{Ar}^* + \text{Ar}^* \rightarrow \text{Ar}^+ + \text{Ar} + e$	1.0×10^{-9}	6
$\text{Ar}^* + \text{Ar}^{**} \rightarrow \text{Ar}^+ + \text{Ar} + e$	1.0×10^{-9}	6,f
$\text{Ar}^{**} + \text{Ar}^{**} \rightarrow \text{Ar}^+ + \text{Ar} + e$	1.0×10^{-9}	6,f
$\text{Ar}_2^* + \text{Ar}_2^* \rightarrow \text{Ar}_2^+ + \text{Ar} + \text{Ar} + e$	5.0×10^{-10}	6
$\text{Xe}^+ + \text{Xe} \rightarrow \text{Xe} + \text{Xe}^+$	3.60×10^{-10}	d
$\text{Xe}^* + \text{Xe} + \text{Xe} \rightarrow \text{Xe}_2^* + \text{Xe}$	$5.0 \times 10^{-32} \text{ cm}^6 \text{ s}^{-1}$	12
$\text{Xe}^{**} + \text{Xe} + \text{Xe} \rightarrow \text{Xe}_2^* + \text{Xe}$	$5.0 \times 10^{-32} \text{ cm}^6 \text{ s}^{-1}$	12,f
$\text{Xe}_2^* \rightarrow \text{Xe} + \text{Xe}$	$7.22 \times 10^7 \text{ s}^{-1}$	12
$\text{Xe}^* \rightarrow \text{Xe}$	$2.34 \times 10^0 \text{ s}^{-1}$	15,g
$\text{Xe}^{**} \rightarrow \text{Xe}^*$	$0.50 \times 10^7 \text{ s}^{-1}$	d
$\text{Xe}^* + \text{Xe}^* \rightarrow \text{Xe}^+ + \text{Xe} + e$	5.0×10^{-10}	12
$\text{Xe}^{**} + \text{Xe}^{**} \rightarrow \text{Xe}^+ + \text{Xe} + e$	5.0×10^{-10}	12,f
$\text{Xe}^+ + \text{Xe} + \text{Xe} \rightarrow \text{Xe}_2^+ + \text{Xe}$	$2.50 \times 10^{-31} \text{ cm}^6 \text{ s}^{-1}$	12

$\text{Xe}^{***} + \text{Xe} + \text{Xe} \rightarrow \text{Xe}_2^* + \text{Xe}$	$5.0 \times 10^{-32} \text{ cm}^6 \text{ s}^{-1}$	d
$\text{Xe}^{***} \rightarrow \text{Xe}$	$5.49 \times 10^6 \text{ s}^{-1}$	d
$\text{Xe}^{**} \rightarrow \text{Xe}^{***}$	$0.50 \times 10^7 \text{ s}^{-1}$	d
$\text{Xe}^{***} + \text{Xe}^{***} \rightarrow \text{Xe}^+ + \text{Xe} + \text{e}$	5.0×10^{-10}	d
$\text{Ar}^* + \text{Xe} \rightarrow \text{Ar} + \text{Xe}^*$	2.10×10^{-10}	6
$\text{Ar}^{**} + \text{Xe} \rightarrow \text{Ar} + \text{Xe}^+ + \text{e}$	2.0×10^{-10}	12
$\text{Ar}^+ + \text{Xe} \rightarrow \text{Ar} + \text{Xe}^+$	4.30×10^{-13}	12
$\text{Xe}^* + \text{Xe} + \text{Ar} \rightarrow \text{Xe}_2^* + \text{Ar}$	$2.30 \times 10^{-32} \text{ cm}^6 \text{ s}^{-1}$	d
$\text{Xe}^{**} + \text{Xe} + \text{Ar} \rightarrow \text{Xe}_2^* + \text{Ar}$	$2.30 \times 10^{-32} \text{ cm}^6 \text{ s}^{-1}$	d
$\text{Xe}^+ + \text{Xe} + \text{Ar} \rightarrow \text{Xe}_2^+ + \text{Ar}$	$2.0 \times 10^{-31} \text{ cm}^6 \text{ s}^{-1}$	d
$\text{Ar}^* + \text{Ar} + \text{Xe} \rightarrow \text{Ar}_2^* + \text{Xe}$	$1.10 \times 10^{-32} \text{ cm}^6 \text{ s}^{-1}$	d
$\text{Ar}^{**} + \text{Ar} + \text{Xe} \rightarrow \text{Ar}_2^* + \text{Xe}$	$1.10 \times 10^{-32} \text{ cm}^6 \text{ s}^{-1}$	d
$\text{Ar}^+ + \text{Ar} + \text{Xe} \rightarrow \text{Ar}_2^+ + \text{Xe}$	$2.0 \times 10^{-31} \text{ cm}^6 \text{ s}^{-1}$	d
$\text{Ar}^* + \text{Xe} + \text{Xe} \rightarrow \text{Xe}_2^* + \text{Ar}$	$1.0 \times 10^{-33} \text{ cm}^6 \text{ s}^{-1}$	d
$\text{Ar}^{**} + \text{Xe} + \text{Xe} \rightarrow \text{Xe}_2^* + \text{Ar}$	$1.0 \times 10^{-33} \text{ cm}^6 \text{ s}^{-1}$	d
$\text{Ar}_2^+ + \text{Xe} \rightarrow \text{Xe}^+ + \text{Ar} + \text{Ar}$	1.25×10^{-9}	16
$\text{Ar}^* + \text{Xe} \rightarrow \text{ArXe}^*$	5.0×10^{-11}	12
$\text{Ar}^{**} + \text{Xe} \rightarrow \text{ArXe}^*$	5.0×10^{-11}	12,f
$\text{Ar}_2^* + \text{Xe} \rightarrow \text{ArXe}^* + \text{Ar}$	5.0×10^{-11}	12
$\text{Ar}^+ + \text{Xe} + \text{Ar} \rightarrow \text{ArXe}^+ + \text{Ar}$	$1.0 \times 10^{-31} \text{ cm}^6 \text{ s}^{-1}$	12
$\text{Ar}^+ + \text{Xe} + \text{Xe} \rightarrow \text{ArXe}^+ + \text{Xe}$	$1.0 \times 10^{-31} \text{ cm}^6 \text{ s}^{-1}$	d
$\text{ArXe}^+ + \text{Xe} \rightarrow \text{Xe}^+ + \text{Ar} + \text{Xe}$	5.0×10^{-10}	12

$\text{ArXe}^+ + \text{Xe} \rightarrow \text{Xe}_2^+ + \text{Ar}$	1.0×10^{-11}	12
$\text{ArXe}^* + \text{Xe} \rightarrow \text{Xe}_2^* + \text{Ar}$	1.0×10^{-10}	12
$\text{ArXe}^* \rightarrow \text{Ar} + \text{Xe}$	$5.0 \times 10^7 \text{s}^{-1}$	12
$\text{Xe}^+ + \text{Ar} + \text{Ar} \rightarrow \text{ArXe}^+ + \text{Ar}$	$1.0 \times 10^{-31} \text{cm}^6 \text{s}^{-1}$	12
$\text{Xe}^* + \text{Ar} + \text{Ar} \rightarrow \text{ArXe}^* + \text{Ar}$	$1.0 \times 10^{-33} \text{cm}^6 \text{s}^{-1}$	12
$\text{Xe}^{***} + \text{Xe} + \text{Ar} \rightarrow \text{Xe}_2^* + \text{Ar}$	$2.30 \times 10^{-32} \text{cm}^6 \text{s}^{-1}$	d
$h\nu + \text{Xe} \rightarrow \text{Xe}^+ + e$	$1.0 \times 10^{-14} \text{cm}^2$	h
$M^+ \rightarrow \text{wall} \rightarrow M$	i	
$M^* \rightarrow \text{wall} \rightarrow M$	i	

^a Rate coefficients have unit of $\text{cm}^3 \text{s}^{-1}$ unless noted otherwise. Electron temperatures are in eV.

^b The rate coefficient was obtained by solving Boltzmann's equation for the EED.

Cross sections for the process are from indicated reference.

^c Cross section and rate coefficient obtained by detailed balance.

^d Estimated.

^e Determined from mobility of ion in Ar.

^f Approximated by analogy.

^g Trapped rate.

^h See text.

ⁱ In wall reactions, all ions recombine to their neutral counterparts and all excited states quench to the ground state.

A.3 References

- ¹ M. Hayashi, Nagoya Institute of Technology Report No, IPPJ-AM-19 (1991).
- ² K. Tachibana, Phys. Rev. A **34**, 1007 (1986).
- ³ D. Rapp and P. Englander-Golden, J. Chem. Phys. **43**, 1464 (1965).
- ⁴ R. H. McFarland and J. D. Kinney, Physical Rev **137**, A 1058 (1965).
- ⁵ L. Vriens, Physics Letters **8**, 260 (1964).
- ⁶ F. Kannari, A. Suda, M. Obara, and T. Fujioka, IEEE J. Quantum Electronics **QE-19**, 1587 (1983).
- ⁷ I. P. Zapesochyni and L. L. Shimon, Opt. Spect. **11**, 155 (1966).
- ⁸ M. A. Biondi, *Principles of Laser Plasmas* (Wiley, New York, 1976).
- ⁹ N. J. Mason and W. R. Newell, J. Phys. B: At. and Mol. Phys. **20**, 1357-1378 (1987).
- ¹⁰ M. Hayashi, J. Phys. D: Appl. Phys. **26**, 581-589 (1983).
- ¹¹ D. J. Eckstrom, H. H. Nakano, D. C. Lorents, T. Rothem, J. A. Betts, M. E. Lainhart, D. A. Dakin, and J. E. Maenchen, J. Appl. Phys. **64**, 1679 (1988).
- ¹² T. H. Johnson, H. E. Cartland, T. C. Genoni, and A. M. Hunter, J. Appl. Phys. **66**, 5707 (1989).
- ¹³ T. Y. Suzuki, Y. Sakai, B. S. Min, T. Takayanagi, K. Wakiya, and H. Suzuki, Phys. Rev. A **43**, 5867 (1991).
- ¹⁴ H. W. Ellis, R. Y. Pai, E. W. McDaniel, E. A. Mason, and L. A. Viehland, At. Data Nucl. Data Tables **17**, 177 (1976).
- ¹⁵ T. Holstein, Phys. Rev. **83**, 1159 (1951).
- ¹⁶ N. Nishida, T. Takashima, F. K. Tittel, F. Kannari, and M. Obara, J. Appl. Phys. **67**, 3932 (1990).